InSAR-Based Structural Monitoring within an Active Caldera: The Case of Diego Armando Maradona Stadium

Tesi di Laurea Magistrale in
Ingegneria dei Sistemi Edilizi

Author: **Alessio Bonzani**

ID: 260232
Advisor: Maria Giuseppina Limongelli
Co-Advisors: Pier Francesco Giordano, Riccardo Liuzzo
Academic year: 2024-2025

Contents

Abstract

Monitoring the integrity of a large structure in a geologically active environment poses significant challenges, as structural behaviour and ground deformation often overlap and interact. This thesis investigates the applicability of satellite-based Interferometric Synthetic Aperture Radar (InSAR) techniques for monitoring the Diego Armando Maradona Stadium, situated within the deforming Campi Flegrei caldera. A central challenge addressed in this work is the separation between ground deformation, driven by the caldera's dynamics, and the structural response of the stadium itself, two processes that spatially overlap and can easily be conflated in satellite observations.

High-resolution COSMO-SkyMed data were processed through a dedicated workflow designed to separate soil subsidence from structural displacements and to reconstruct the deformation components relevant to the roof's radial steel trusses. Two approaches for modelling and removing the regional ground motion were implemented.

By integrating ascending and descending satellite geometries and projecting the line of sight measurements onto beam-aligned local reference systems, the study captured direction dependent deformation patterns and identified clear seasonal cycles attributable to thermal expansion of the steel elements, extending techniques usually applied to linear infrastructures such as bridges and viaducts.

Overall, the findings confirm the potential of InSAR as a non-invasive and reliable tool for the continuous monitoring of the stadium's elliptical roof structure in a dynamic geological setting.

Keywords: Spaceborne InSAR Monitoring, Active Caldera, Structural Health Monitoring, Displacements, Subsidence, Stadium, Cosmo-SkyMed.

Abstract in lingua italiana

Il monitoraggio dell'integrità di una grande struttura in un contesto geologicamente attivo rappresenta una sfida significativa, poiché le deformazioni strutturali e i movimenti del terreno tendono a sovrapporsi e a interagire.
Questa tesi indaga l'applicabilità delle tecniche satellitari Interferometric Synthetic Aperture Radar (InSAR) per il monitoraggio dello Stadio Diego Armando Maradona, situato all'interno della caldera dei Campi Flegrei. Una delle difficoltà centrali affrontate consiste nella separazione tra le deformazioni del suolo, legate alla dinamica del sistema vulcanico, e la risposta strutturale dello stadio, due processi che si sovrappongono spazialmente e che possono facilmente essere confusi nelle osservazioni satellitari.
I dati ad alta risoluzione della costellazione COSMO-SkyMed sono stati elaborati attraverso un workflow dedicato, sviluppato per distinguere i fenomeni di subsidenza dagli spostamenti propri della struttura e per ricostruire le componenti di deformazione associate alle travi radiali in acciaio della copertura. Sono stati implementati due approcci per modellare e rimuovere il contributo deformativo di origine geologica.
L'integrazione delle geometrie di acquisizione ascendente e discendente, unita alla proiezione delle misure lungo linea di vista su sistemi di riferimento locali allineati alle travi, ha consentito di evidenziare deformazioni dipendenti dall'orientazione degli elementi e di identificare chiari cicli stagionali attribuibili alla dilatazione termica delle componenti metalliche, estendendo le tecniche applicate a infrastrutture lineari come ponti e viadotti.
Nel complesso, lo studio conferma il potenziale dell'InSAR come strumento non invasivo e affidabile per il monitoraggio continuo della copertura ellittica dello stadio in un contesto geologico dinamico.

Parole chiave: Monitoraggio Satellitare InSAR, Caldera Attiva, Monitoraggio della salute strutturale, Spostamenti, Subsidenza, Stadio, Cosmo-SkyMed.

List of Figures

List of Tables

Glossary of acronyms

Several specialised acronyms appear in the text. The table below provides their definitions to support consistent interpretation.

ALD	**A**zimuth **L**ooking **D**irection
ASI	**I**talian **S**pace **A**gency
COSMO	**C**onstellation **O**f **S**mall **S**atellites for the **M**editerranean basin **O**bservation
CSG	**C**OSMO **S**econd **G**eneration
CSK	**C**OSMO **Sk**yMed
DEMs	**D**igital **E**levation **M**odels
DInSAR	**D**ifferential **In**terferometric **S**ynthetic **A**perture **R**adar
DS	**D**istributed **S**catterers
EO	**E**arth **O**bservation
ENVISAT	**EN**vironmental **SAT**ellite
ERS	**E**uropean **R**emote **S**ensing
InSAR	**I**nterferometric **S**ynthetic **A**perture **R**adar
LOS	**L**ine **O**f **S**ight
MT-DInSAR	**M**ulti **T**emporal **D**ifferential **In**terferometric **S**ynthetic **A**perture **R**adar
PCC	**P**earson **C**orrelation **C**oefficient
PS	**P**ersistent **S**catterers
PSI	**P**ersistent **S**catterer **I**nterferometry
RADAR	**R**adio **D**etection **A**nd **R**anging
RAR	**R**eal **A**perture **R**adar
RMSE	**R**oot **M**ean **S**quare **E**rror
RT	**R**evisit **T**ime
SAR	**S**ynthetic **A**perture **R**adar
SB	**S**mall **B**aseline
SBAS	**S**mall **B**aseline **S**ubset
SHM	**S**tructural **H**ealth **M**onitoring
SLC	**S**ingle **L**ook **C**omplex

1 | Introduction

Ageing, material degradation, increasing operational demands and environmental loading pose growing challenges to the safety and serviceability of built assets [1], [2]. These challenges concern a wide spectrum of structures, ranging from transportation infrastructure and public facilities to large assembly buildings such as stadiums. Although their societal roles differ, these assets share a common requirement: their structural condition must be understood and managed to ensure safety, functionality and continuity of service.

Among the measurable indicators of structural behaviour, displacement plays a central role. Changes in geometry over time may result from settlements, differential support movements, thermal expansion and contraction, or variations in loading conditions. In some cases, these effects correspond to normal structural response; in others, they may indicate the development of damage or loss of performance. Displacement monitoring is therefore essential for distinguishing between acceptable behaviour and conditions requiring further investigation. In this context, the ability to observe slow, spatially distributed deformation over extended periods represents a significant advantage for structural assessment.

Structural Health Monitoring (SHM) provides tools for collecting and analysing information about structural performance. Traditional contact sensors offer high accuracy but are often limited to specific instrumented points and require installation, maintenance and access to the structure [3]. Remote sensing techniques offer a complementary perspective. In particular, satellite-based Interferometric Synthetic Aperture Radar (InSAR) enables the measurement of ground and structural displacements with millimetric precision, wide spatial coverage and consistent temporal sampling. These characteristics make InSAR particularly suitable for detecting long-term deformation patterns and for monitoring assets embedded in complex geological environments.

The geological context may significantly influence the observed displacement time series. In volcanic calderas such as the Naples and Campi Flegrei area, ground motion driven by magmatic, hydrothermal or tectonic processes can generate persistent and spatially variable deformation [4]. For structures located within such environments, the measured displacement may reflect not only structural behaviour but also ground movements. Distinguishing between these contributions is therefore essential to avoid misinterpretation and to support informed decision-making.

1.1. Aims and Purpose of the study

Satellite-based InSAR is increasingly applied to the monitoring of civil structures; however, its use for structural assessment and damage detection is often limited by difficulties in data interpretation. Displacement time series derived from Persistent Scatterers (PSs) may be dominated by components that are not directly related to structural health, but rather to external factors such as temperature effects, soil movements, or regional subsidence. When these contributions are not adequately identified and accounted for, the resulting displacement signal may be misinterpreted, leading to inappropriate assessments and suboptimal prioritisation of inspections or interventions.

This challenge becomes particularly critical in volcanically active areas such as the Naples and Campi Flegrei caldera, where ground deformation driven by magmatic, hydrothermal, and tectonic processes can reach magnitudes significantly larger than typical structural displacements. In such conditions, the structural response of a structure may represent only a minor component of the total measured deformation. The separation of environmental and soil-induced movements from structure-scale behaviour therefore becomes a prerequisite for any reliable structural interpretation.

Within this context, the present study investigates the deformation behaviour of the roof of the Diego Armando Maradona Stadium using high-resolution COSMO-SkyMed Second Generation (CSG) data. The primary aim of the thesis is to develop and evaluate methodologies capable of separating regional ground deformation from building-scale displacements, and to quantify how different compensation strategies influence the deformation patterns ultimately attributed to the structure. Ascending and descending viewing geometries are jointly exploited to reconstruct three-dimensional displacement fields, thereby improving the physical interpretability of the observed response.

1.2. Innovative Aspects of the Research

The main novel aspect of this thesis concerns the development of approaches for removing large-scale environmental deformation from InSAR time series, with particular attention to the strong subsidence affecting the Naples and Campi Flegrei area. While satellite-based monitoring has been increasingly applied to civil structures, the separation of regional ground motion from structure-related deformation remains a critical issue, especially in volcanically active environments where background movements are significant and spatially heterogeneous.

Two alternative strategies for modelling and subtracting regional deformation are presented. The analysis focuses on how the choice of compensation method influences the residual displacement field attributed to the structure. The results show that different correction schemes

may lead to noticeably different interpretations of the structural response, highlighting the need for careful assessment of the adopted approach.
An additional aspect concerns the treatment of structural elements with different orientations. Owing to the elliptical geometry of the stadium, the primary roof beams are not aligned along a common global direction. Each element is therefore analysed within a locally defined coordinate system aligned with its longitudinal axis. The corrected Line-Of-Sight (LOS) measurements are projected according to the local orientation of each member, and the influence of this orientation on the reconstructed displacement components is explicitly examined. This procedure allows the deformation to be interpreted consistently along individual elements and clarifies how directional sensitivity affects the reconstructed displacement field. It is particularly relevant for structures characterised by curved geometries and varying alignment of structural members, where the use of a single global reference frame may lead to ambiguous or physically inconsistent interpretations.

1.3. Thesis Roadmap

The thesis is structured into five chapters:

- *Chapter 1:* introduces the topic of InSAR-based structural monitoring, defines the research objectives and questions, and outlines the main contributions of the work.
- *Chapter 2:* presents the fundamentals of radar remote sensing and InSAR, reviewing the main satellite missions and multi-interferogram techniques, together with their limitations and sources of error.
- *Chapter 3:* describes the processing methodology adopted in the thesis, including the integration of multiple LOS datasets for deformation reconstruction and the use of locally defined reference systems to account for the varying orientation of longitudinal structural elements. Also, it addresses the modelling and removal of regional ground deformation within the InSAR framework, implementing two approaches for estimating the regional trend.
- *Chapter 4:* applies the proposed methodology to the roof structure of the Diego Armando Maradona Stadium, presenting the datasets, processing steps, displacement time series, and uncertainty assessment.
- *Chapter 5:* summarises the main findings, discusses the limitations of the study, and outlines directions for future research.

2 | Fundamentals of Satellite Radar Data

The ability to detect ground surface displacements caused by slow deformation processes, and to monitor their evolution over time, at any hour of the day and regardless of weather conditions, represents a fundamental opportunity for supporting the protection and management of both natural and built environments. In the past few decades, Earth Observation (EO) has benefited from the rapid development of satellite remote sensing technologies, which have significantly enhanced our capacity to analyse and understand environmental, geological, and infrastructural dynamics. Among these technologies, Synthetic Aperture Radar (SAR) systems have become essential tools due to their capability to acquire data independently of illumination conditions, while providing extensive spatial coverage and revisit times ranging from a few hours to several weeks [5].

The evolution of satellite missions has played a crucial role in the development of interferometric techniques. Early ESA missions such as ERS 1 and ERS 2 introduced the operational use of C band SAR for Earth monitoring, laying the groundwork for the first interferometric applications. The subsequent ENVISAT mission, equipped with the ASAR sensor, marked a significant improvement in spatial resolution and acquisition frequency. Later, the Italian COSMO SkyMed constellation, operating in X band, further expanded monitoring capabilities through shorter revisit times and enhanced operational flexibility. More recently, the Sentinel 1 constellation, with its open access data policy, has made unprecedented volumes of SAR imagery available, greatly supporting both scientific research and operational monitoring activities.

The chapter opens by introducing the fundamental principles of satellite radar interferometry, starting from the basics of radar remote sensing and the core concepts behind InSAR. It explains how electromagnetic waves interact with the Earth's surface, how acquisition geometry influences the recorded signal, and how these elements combine to produce high resolution SAR images that form the basis of interferometric analysis.

Building on these foundations, the chapter then offers an overview of the major SAR missions that have shaped the development of interferometric techniques. It retraces the progression from the pioneering ERS 1 and ERS 2 satellites, through the improved observational capabilities of ENVISAT, to the high frequency acquisitions enabled by the COSMO SkyMed constellation. The section discusses the impact of Sentinel 1, whose open access data policy has made SAR

observations widely available to both researchers and operational users.
The discussion progresses to the methodologies used to process SAR data. These techniques enable the generation of spatially dense deformation velocity maps and displacement time series, making them particularly powerful for monitoring slow moving processes that affect both natural environments and man made structures.

2.1. Satellite Radar Interferometry

Compared to traditional in-situ monitoring methods, satellite remote sensing offers minimal environmental impact, reduced operational costs, and the invaluable advantage of accessing large historical data archives, enabling the reconstruction of past deformation processes even before ground based instruments are installed.

2.1.1. Radar remote sensing

Remote sensing is defined as the set of techniques that allow the observation and study of regions of the Earth's surface through the interaction of electromagnetic waves with objects located at a considerable distance from the observer. The advantage of remote sensing, which has driven its widespread adoption in EO, lies primarily in its ability to perform remote observations with large spatial coverage (even tens of thousands of km^2) and with temporal revisit frequencies ranging from a few hours to several tens of days. This results in an almost negligible environmental impact and limited monitoring costs when compared to in-situ methods, which, although capable of accurate measurements, require direct access to sites that can be difficult to reach due to adverse climatic or environmental conditions (e.g., polar ice caps, volcanic craters, landslide areas) [6], [7].
Sensors used in the various remote sensing techniques can be classified as passive or active according to their operating principle: passive sensors exploit the natural electromagnetic radiation emitted by bodies or the solar radiation reflected by them, in the absence of a transmitted signal; active sensors, instead, are equipped with both a transmitter and a receiver (antenna) that, by sending an appropriate signal, "illuminate" the area of interest and record the backscattered information from the scene. Among active remote sensing instruments, satellite RADAR (RAdio Detection and Ranging) systems are the most widely used for monitoring the biogeophysical parameters of the Earth's surface [8]. Radar is an active remote sensing system operating in the microwave band (typical wavelengths from 1 m to 1 mm, corresponding to frequencies from about 300 MHz to 300 GHz), in which an electromagnetic signal is emitted by a transmitting antenna and illuminates the various targets in the observed scene; part of the incident signal is absorbed by the illuminated area, part is reflected and a portion is re-sent

toward the satellite (backscattered signal), where it is recorded by the receiving antenna as illustrated in Figure 2.1. The echoes recorded by the receiving antenna are then converted to digital format and subsequently processed to form a radar image. The radar satellite systems

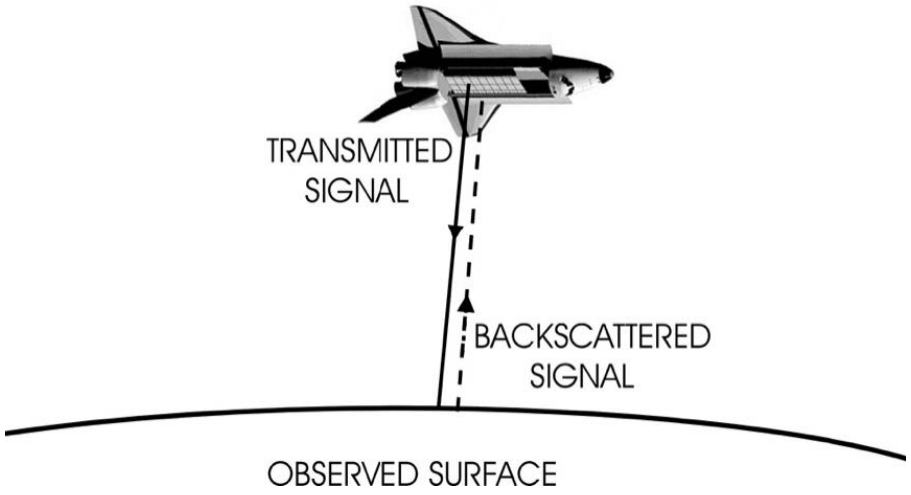

Figure 2.1: Schematic representation of the operating principle of an active remote sensing system [9].

most used for surface monitoring orbit the Earth on near polar trajectories (sun synchronous orbits, defined as geocentric orbits with altitude and inclination values that ensure the satellite passes over the same ground point at the same local solar time) at altitudes between 500 and 800 km above the Earth's surface. As shown in Figure 2.2. they travel on tracks slightly inclined with respect to the meridians (by a few degrees), completing half an orbit from the North Pole to the South Pole (descending pass) and the other half from the South Pole to the North Pole (ascending pass).

During flight along their orbit, the radar sensors mounted on the satellite emit electromagnetic signals along the LOS direction, within a given frequency band, and acquire the backscattered echoes, recorded as time delays and thus as distances between ground points and the sensor. These data are then processed through procedures that elaborate the set of recorded digital echoes until an image of the observed area is obtained. The combination of the satellite's orbital motion with the Earth's rotation allows radar images of the same area to be acquired at different times; the time the satellite takes to revisit the same area is called the Revisit Time (RT) [5].

Radar systems travel along the flight direction and transmit electromagnetic pulses that illuminate a portion of the Earth's surface known as the footprint, whose extent develops both parallel and perpendicular to the satellite's flight path. The acquisition geometry of a radar satellite can be described in cylindrical coordinates (x, r, θ): the coordinate (x), called azimuth (AZ), is aligned with the satellite's flight line, which forms a small angle (ϕ, the heading angle) with the meridians; the coordinate (r), called slant range or simply range (RG), represents the

distance along the LOS between the sensor and a ground point, i.e., the pointing direction along which signals are transmitted and received and that interact with the targets in the illuminated area. The third coordinate (θ), known as off nadir or look angle, is the angle between the vertical and the line of sight and varies with sensor type and operating mode (for example, about 23° for ERS sensors and between 15° and 45° for COSMO SkyMed). The radar's side looking viewing geometry resolves the left/right ambiguity for equirange points objects at the same distance from the sensor [10].

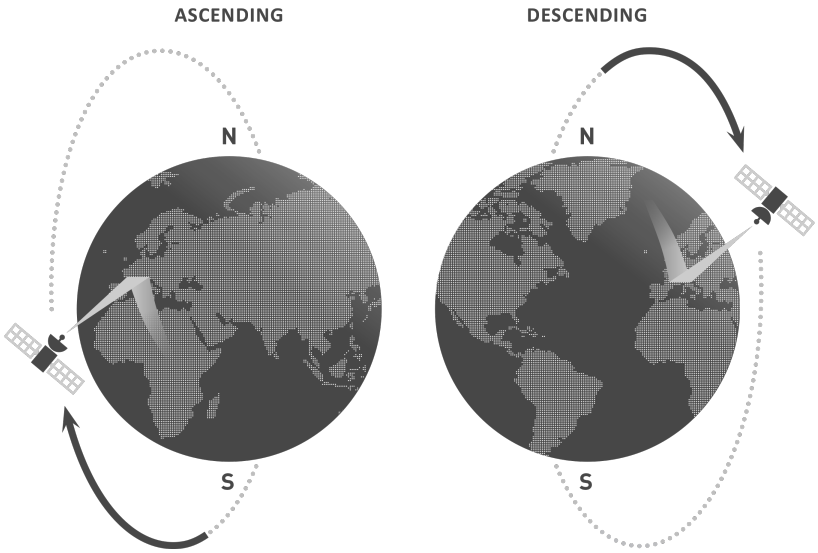

Figure 2.2: Schematic representation of satellite image acquisition from ascending and descending orbital passes [11].

The ground projection of the range direction is called ground range, while the footprint width on the ground is referred to as the Swath Width (the ground distance between the near range and far range points). Figure 2.3 illustrates this geometry; note that, for clarity, the figure may distort the true proportions of the angle between the near range and far range lines. In practice, that angular variation is often small enough that the look angle (θ) evaluated at scene center (mid range) suffices to describe the system.

After the antenna records the echoes, the raw data undergoes processing (commonly called focusing) to produce the radar image. The image is a matrix of pixels defined along azimuth and slant range, the so called radar coordinates. The range resolution (Δr) is the minimum separation in slant range required for two ground objects to be distinguished as separate targets; it is given by the following relation:

$$\Delta r = c \cdot \frac{\tau}{2} \cong \frac{c}{2\Delta f} \tag{1}$$

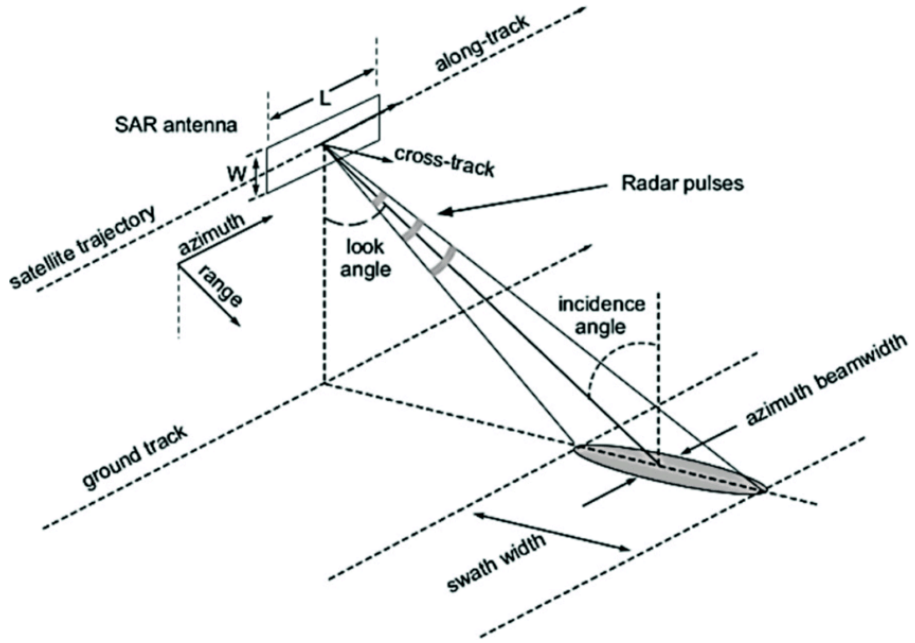

Figure 2.3: Geometry of radar signal acquisition [12].

From this expression it is clear that (Δr) depends on the speed of light (c) and on the pulse duration (τ), the factor 2 accounting for the two way travel of the electromagnetic wave. Since (τ) is the inverse of the signal bandwidth (Δf), achieving fine range resolution requires a wide band signal, i.e. a short pulse. However, because the propagating signal suffers attenuation, sufficient transmitted power is needed, which is obtained with pulses of non negligible duration. To reconcile wide bandwidth and adequate transmitted energy, remote sensing radars use frequency modulated pulses, such as the chirp (a signal whose frequency varies linearly with time), which provide large bandwidths together with sufficiently long pulse durations.
Similarly, two points are resolved in azimuth if they do not both lie within the antenna beam. The azimuth resolution (Δx) is therefore related to the antenna beamwidth and is expressed by:

$$\Delta x = r \cdot \frac{\lambda}{L} \tag{2}$$

where (r) is the sensor to target distance, (λ) the wavelength, (L) the physical antenna length, and ($\frac{\lambda}{L}$) the angular extent (3 dB beamwidth) of the azimuthal lobe. For a Real Aperture Radar (RAR), azimuth resolution is proportional to the distance (r) and to the wavelength, and inversely proportional to the antenna length; consequently, on satellite platforms the RAR typically yields coarse azimuth resolution (on the order of tens of kilometres), much worse than range resolution (on the order of metres).
To overcome this limitation, SAR systems exploit the antenna motion along the flight path to

improve azimuthal spatial resolution without increasing the physical antenna size, by synthesising a larger effective aperture. The basic idea is that a target remains within the antenna beam for a certain time while the radar observes it repeatedly from successive positions along the flight line: at each position the antenna transmits a pulse and receives its echo, and the antenna motion synthesises an array of elementary antennas of effective length much greater than the real antenna (a synthetic array), thus producing a very large effective aperture.
In SAR sensors the backscattered echoes are recorded coherently, that is, both amplitude and phase are preserved, and a sophisticated processing chain applied to the collected echoes yields the SAR image, whose azimuth resolution is given by the following formula:

$$\Delta x = \frac{L}{2} \tag{3}$$

Note that in this expression the dependence on wavelength and on the sensor to target distance present in the RAR case disappears; moreover, reducing the real antenna length in azimuth broadens its beam and thus increases the extent of the synthetic aperture, improving the achievable spatial resolution. The enhanced resolution provided by SAR necessarily requires a dedicated processing stage: focusing the raw data produces a complex image known as a Single Look Complex (SLC) (see Figure 2.4) [5].

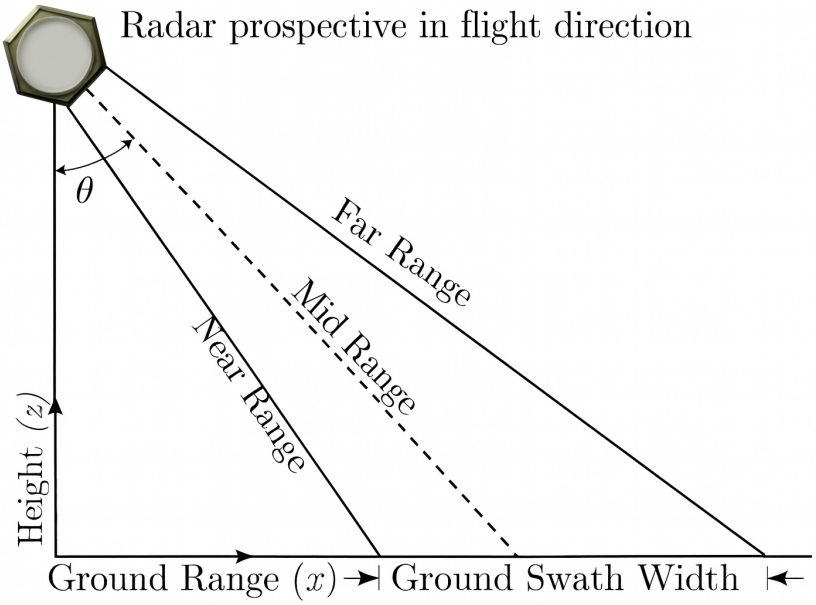

Figure 2.4: Schematic representation of the side-looking radar acquisition geometry in the range plane [13].

A SAR image is therefore represented digitally as an n times m matrix of pixels in radar coordinates, each pixel characterised by an amplitude (E) and a phase (γ), which carry the

information related to the backscattered signals from the ground scene (alternatively, pixels can be expressed by their real and imaginary parts). SAR images are coherent: the amplitude encodes the backscatter intensity, linked to the scene reflectivity, while the phase depends on the geometric and electromagnetic properties of the observed scene and on the distance between sensor and ground targets.

SAR images, typically displayed in grayscale, convey rich radiometric information: variations in brightness reflect differences in the scene's ability to backscatter the radar pulse, with brighter tones indicating higher reflectivity. This radiometric response depends on observation geometry and signal properties but is strongly governed by the physical and structural characteristics of the illuminated surfaces. Rough textures tend to produce strong backscatter and appear bright, whereas smooth surfaces, for example roads and highways, return little energy and appear dark. Vegetation usually yields a uniform grey tone, although density and species composition modulate the backscatter intensity. Slopes facing the sensor reflect more energy and thus look brighter than slopes inclined away, and urban features, buildings and paved areas, often generate very bright returns because of multiple reflections that return to the sensor with limited attenuation.

Because SAR senses the scene obliquely rather than vertically, its images differ both radiometrically and geometrically from optical imagery, and these differences must be considered during interpretation. Even without topography, the ground range projection varies from near to far range: a given slant range pixel projects to a larger ground range extent towards the near range and to a smaller one near the far range, so ground range resolution is generally poorer in the near range. This effect, together with the side looking geometry, produces characteristic perspective distortions that are intrinsic to radar observations.

Terrain morphology and slope introduce further, well defined geometric deformations on the azimuth-range plane: foreshortening, layover and shadowing. Foreshortening compresses or stretches resolution cells depending on the local slope relative to the horizontal, often increasing brightness where many reflecting facets contribute to the return. Layover is an extreme foreshortening case that occurs when slope exceeds the look angle: higher terrain elements are mapped at shorter slant ranges and thus appear reversed in radar coordinates, inverting the true topographic order. Shadowing arises where parts of the terrain are occluded from the radar line of sight and therefore receive no illumination, appearing as uniformly dark areas in the image.

These combined radiometric and geometric effects are evident in real SAR scenes: coastlines, water bodies and rocky outcrops show markedly different grey levels according to their backscatter, while volcanic edifices and steep reliefs clearly illustrate foreshortening, layover and shadowing along the radar line of sight [5].

2.1.2. Principles of Interferometric SAR (InSAR)

SAR images are processed so that both amplitude and phase information are preserved for every pixel. The amplitude represents the portion of the incident electromagnetic field that is backscattered by scene objects toward the sensor, while the phase carries essential information for interferometric methods because it encodes the two way path travelled by the signal between sensor and target. In particular, the phase term (γ) of a SAR image can be expressed by the following relation, which includes the wavelength (λ) and the sensor to target distance (r), together with a phase contribution (Ψ) due to target reflectivity, an atmospheric term (α) accounting for propagation effects, and a noise term (n) representing the unavoidable measurement errors of the acquisition system (e.g. curvature of the Earth, signal to noise limitations, and instrumental noise):

$$\gamma = \Psi + \frac{4 \cdot \pi}{\lambda} \cdot r + \alpha + n \tag{4}$$

However, the phase measured in a single acquisition is of limited direct use because the various contributions are mixed and the backscatter component is often random, making it difficult or impossible to separate the individual terms. To exploit the phase information contained in each pixel, it is therefore necessary to combine, i.e. interfere, that image with at least one other acquisition of the same area. This approach, known as Interferometric Synthetic Aperture Radar (InSAR), is the fundamental technique for detecting surface changes with high precision. When the scattering properties of the targets remain stable between acquisitions, the interferometric phase ($\Delta\gamma$) can be defined as the pixel wise phase difference between the two images; this quantity is wrapped within the interval $[-\pi, +\pi]$.
Rearranging the previous expression yields the following form:

$$\Delta\gamma = \frac{4 \cdot \pi}{\lambda} \cdot \Delta r \tag{5}$$

From the interferometric phase expression, it becomes clear that, after removing the reflectivity related contributions, the phase depends primarily on the optical path difference (Δr) between sensor and target (apart from residual atmospheric and noise terms) [5], [14]. Moreover, if the two SAR images are acquired from different sensor positions, the interferometric phase contains not only the component associated with any surface deformation occurring between acquisitions but also a component related to terrain elevation.
Consequently, InSAR is not only a powerful tool for measuring ground motion over time but also enables the retrieval of interferometric Digital Elevation Models (DEMs) and the reconstruction of the scene topography.

2.2. Satellite Missions and Sensors

Over the past thirty years, the fleet of satellites dedicated to EO has expanded significantly, introducing sensors with a wide range of characteristics in terms of spatial resolution, wavelength, revisit time and ground coverage [5]. Figure 2.5. provides a schematic representation of the sensors that have been operational since 1991, organized according to the ground footprint (swath) and their revisit intervals.

Below is a concise summary of the main SAR sensors widely used today for interferometric analyses: the ERS 1, ERS 2 and ENVISAT satellites developed by the European Space Agency (ESA); the COSMO SkyMed constellation, first (CSK) and second generation (CSG), developed by the Italian Space Agency in cooperation with the Ministry of Defence; and the Sentinel 1 (S1) constellation, developed by ESA within the European Copernicus programme.

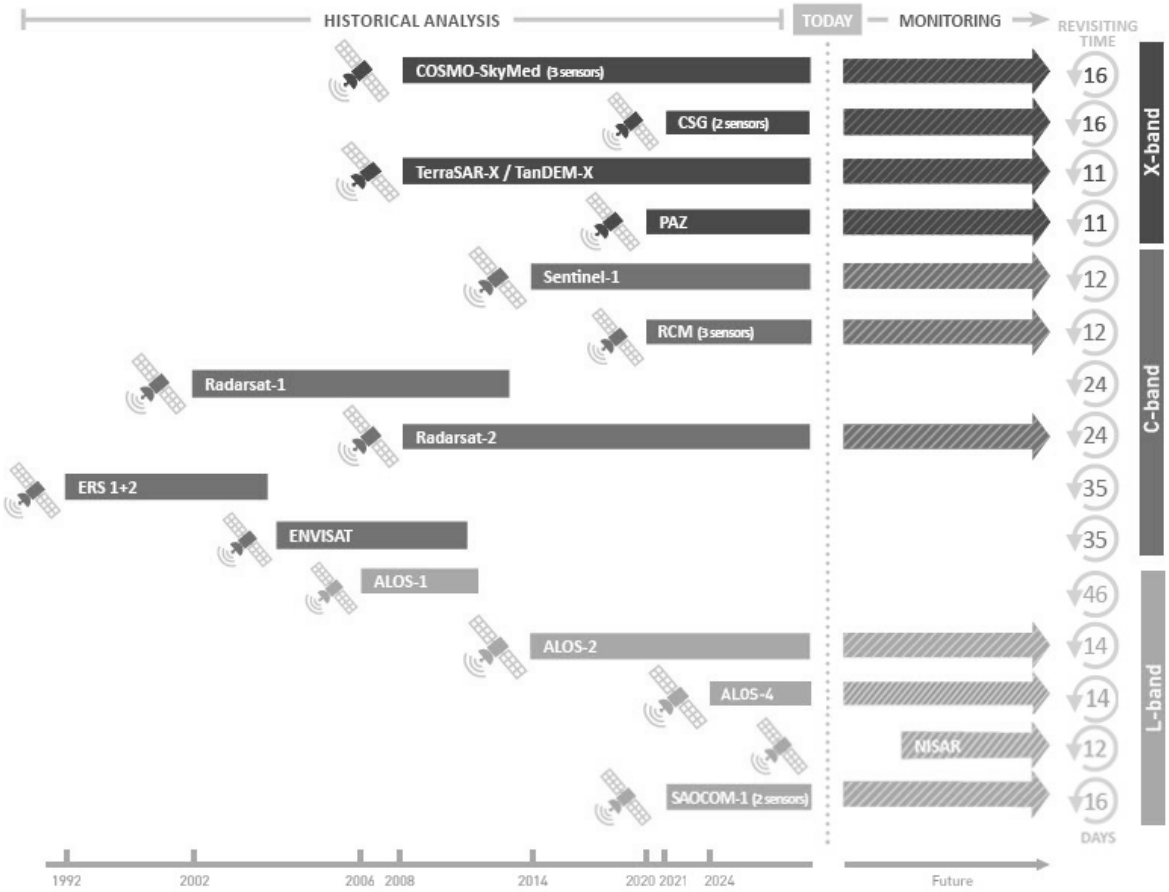

Figure 2.5: Main operational (or previously operational) SAR sensors since 1991. Although the following paragraphs exclusively describes the ERS, ENVISAT, COSMO-SkyMed and Sentinel-1 constellations, the image also includes other SAR sensors [11].

2.2.1. ERS 1/2 and ENVISAT

The three satellites ERS 1, ERS 2 and ENVISAT were developed by ESA [15]. The first, ERS 1 (European Remote Sensing satellite), remained operational from July 1991 to March 2000, well beyond its expected lifetime [16]. It carried a suite of instruments for observing various environmental parameters (water, land, ice and atmosphere), including a C band SAR sensor (wavelength $\lambda = 5.6$ cm) that acquired images with a revisit time of 35 days over the same ground area.
In April 1995 ESA launched ERS 2, a twin of ERS 1, which operated until September 2011. ERS 2 shared the same near polar orbit as ERS 1 but was phased by 24 hours, so that the same ground scene was observed by the two satellites one day apart, while each individual satellite revisited the same area every 35 days.
Subsequently, ESA developed and launched ENVISAT (Environmental Satellite), which, like its predecessors ERS 1 and ERS 2, was equipped with, among other instruments, a C band SAR sensor (wavelenghet $\lambda = 5.6$ cm) and had a revisit time of 35 days. ENVISAT was operational from March 2002 to April 2012 [17]. In general, these three ESA satellites acquired primarily in Stripmap mode, with spatial resolution on the order of 5 m in azimuth and about 20 m in ground range. The ground footprint extended roughly 100 km in range, and data were collected along both ascending and descending orbital tracks. For distribution and user access, each track was divided into equally sized frames, each covering approximately a 100 km $\times$ 100 km ground area [5], [18].

2.2.2. COSMO-SkyMed

The COSMO SkyMed constellation (COnstellation of small Satellites for the Mediterranean basin Observation, often abbreviated as CSK), developed by the Italian Space Agency (ASI) in cooperation with the Ministry of Defence, is the first EO mission conceived for dual civil and military use [19].
Originally composed of four identical satellites equipped with an X band SAR sensor (wavelength $\lambda = 3.1$ cm), the constellation was deployed progressively: the first satellite was launched on 7 June 2007, the second on 9 December 2007, the third on 25 October 2008, and the fourth on 5 November 2010. Currently all CSK satellites are operational except the third (CSK3), which, following a de orbiting procedure initiated in May 2022, was permanently shut down in October 2022.
As the operational lifetime of the four first generation CSK satellites approached its end, the first two satellites of the second generation COSMO SkyMed Second Generation (CSG) constellation were launched in December 2019 and January 2022. The CSG constellation is intended

to ensure continuity of operations with the existing CSK assets while providing improved image quality and enhanced operational capabilities.
The revisit interval for each satellite in both the CSK and CSG constellations is 16 days; the phasing between satellites allows, when all four first generation CSK satellites are fully operational, an average revisit of the same ground scene every four days.
CSK and CSG satellites support multiple acquisition modes; the most used are Stripmap HIMAGE, offering approximately 3 m x 3 m spatial resolution (azimuth × range) with a swath of about 40 km in range, and Spotlight, which achieves sub metre spatial resolution (better than 1 m) with a swath of roughly 10 km x 10 km (range × azimuth).

2.2.3. Sentinel-1

The Sentinel 1 constellation initially comprised two satellites, both operating on near polar orbits and each equipped with a C band SAR sensor (wavelenght $\lambda = 5.56$ cm). The first, Sentinel 1A (S-1A), was launched in April 2014; its twin, Sentinel 1B (S-1B), was launched in April 2016 but became non operational in December 2021 due to a failure in the radar instrument power supply. The revisit time for a single satellite is 12 days; when both satellites were fully operational (2016–2021) the effective revisit dropped to 6 days, a benefit no longer available after the loss of Sentinel 1B.
Currently Sentinel 1A remains fully operational (12 day revisit), and plans exist to launch a replacement, Sentinel 1C (expected in 2024), to ensure mission continuity.
Sentinel 1 satellites are designed for land acquisitions in TOPS mode (Terrain Observation by Progressive Scans), which enables the Interferometric Wide Swath (IWS) acquisition. IWS provides approximately 15 m spatial resolution in azimuth and about 4 m in range; each illuminated ground slice covers roughly 200 km in azimuth by 250 km in range.
The constellation operates according to a scheduled acquisition plan aimed at building robust image archives over large land areas for long term monitoring.

2.3. Processing Techniques

2.3.1. Differential Interferometry SAR (DInSAR)

Differential Interferometric Synthetic Aperture Radar (DInSAR) is a microwave remote sensing technique that quantifies surface displacement by comparing the phase of two SAR images acquired over the same area at different times and, possibly, from slightly different orbital positions (see Figure 2.6). One image is designated master and the other slave; the time between acquisitions is the temporal baseline and the orbital separation the spatial baseline [20]. After removing the scene's mean topography using an external DEM, the phase difference yields an interferogram, initially a wrapped phase field in the interval $[-\pi, +\pi]$, whose cycles of 2π correspond to LOS displacements of $\lambda/2$; recovering absolute phase therefore requires phase unwrapping.

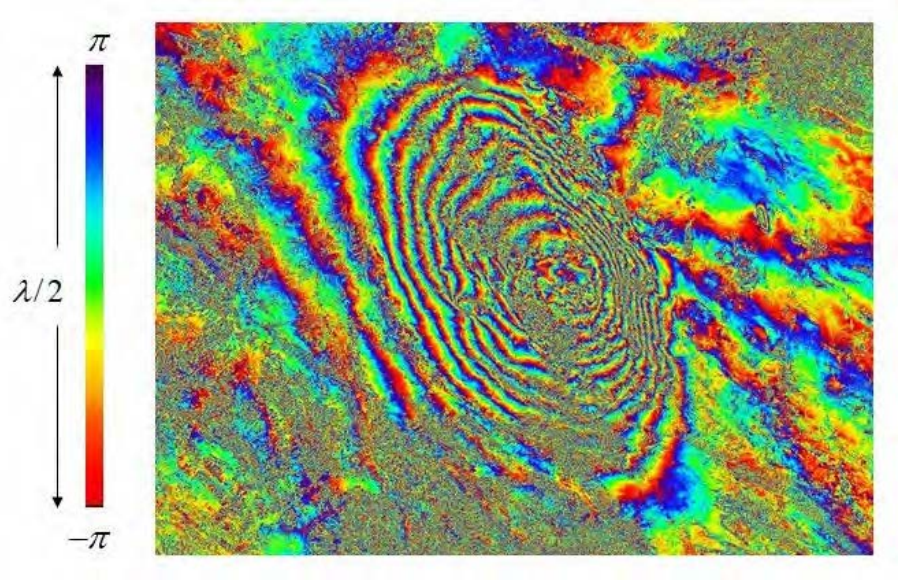

Figure 2.6: Co-seismic interferogram of the earthquake that struck the city of L'Aquila on 6 April 2009, obtained from COSMO-SkyMed SAR imagery [21].

DInSAR measurements are differential in time and space, referenced to a chosen date and stable ground point, and can achieve accuracies from centimetres down to millimetres (fractions of the sensor wavelength). The technique is widely used to map co-seismic deformation, subsidence, landslides, volcanic unrest and other geodynamic processes, producing high density displacement maps at relatively low cost. Result quality, however, depends critically on image coherence and on the ability to separate deformation phase from other contributions: residual topographic errors (DEM inaccuracies), orbital errors, atmospheric delays, and noise can all contaminate the signal [5].

Coherence is reduced by temporal decorrelation (longer intervals, vegetation, snow), geometric decorrelation (large normal baselines), local topography and variable surface electromagnetic properties; it is typically higher over urban areas and exposed rock and can be improved by using longer radar wavelengths (e.g. L band versus X band). Geometric distortions and decorrelation therefore limit DInSAR applicability in some environments, while the growing availability of processing tools and platforms (e.g. ESA SNAP) has made the technique increasingly accessible to practitioners [22].

2.3.2. Multi Temporal Differential Interferometry SAR

Multi Temporal Differential Interferometric SAR (MT-DInSAR) represents the natural evolution of single pair DInSAR toward robust, temporally resolved monitoring of surface deformation. Instead of relying on one or a few interferograms, MT-DInSAR analyses large stacks of SAR images and their differential interferograms to extract time series of displacement and maps of average velocity. By jointly modelling interferometric phase in space and time and by exploiting redundancy across many acquisitions, MT-DInSAR can better separate true deformation from residual topographic errors, orbital inaccuracies and atmospheric delays, and it supports more reliable phase unwrapping than single pair approaches.

Two families dominate operational practice because they embody different assumptions about the scattering behaviour of the ground. Persistent Scatterer Interferometry (PSI) assumes a single, temporally stable scatterer per resolution cell and typically works at full spatial resolution; this makes PSI highly precise where persistent targets exist (cities, exposed rock) and tolerant of large temporal and spatial baselines, but it yields sparse point coverage in vegetated or rural areas and is less suited to strongly non linear deformation histories. Small Baseline (SB) methods assume distributed scattering within the resolution cell, select interferogram pairs that minimize temporal and normal baselines to limit decorrelation, and often apply multi look averaging to boost phase SNR; SB approaches increase coherent point density in non urban areas but require careful interferogram selection, multiple masters or subsets, and post processing to merge independent subsets into a consistent time series.

Practically, MT-DInSAR delivers highly valuable, dense deformation records for subsidence, co seismic displacement, landslides and volcanic unrest, often achieving precision down to fractions of the radar wavelength. These benefits come at the cost of greater algorithmic complexity, longer runtimes and more demanding error modelling, including explicit treatment of atmospheric artefacts and DEM/orbital residuals. Recent developments blend PSI and SB ideas (multi scale or hybrid workflows) and extend capabilities with techniques such as TomoSAR to resolve vertical structure and increase point density in challenging environments [23].

The main advanced MT-DInSAR techniques differ by their scattering model and by the strat-

egy used to select and combine interferograms [24].

PSInSAR (Permanent Scatterers) identifies and exploits temporally stable scatterers (buildings, towers, rock outcrops) by comparing many images against a single master to produce very precise time series and to estimate atmospheric contributions via spatial interpolation; thanks to the robustness of Permanent Scatterers, PSInSAR is especially effective in urban and industrial settings where the radar response is stable over time and enables continuous monitoring of critical infrastructure, and on suitably large datasets can achieve accuracies on the order of $\pm$ 1 mm/yr for mean velocity and $\pm$ 5 mm for displacement [25].

SBAS (Small Baseline Subset), by contrast, builds numerous interferograms with small temporal and spatial baselines and solves an overdetermined system to produce two scale velocity maps (regional, medium resolution and local, full resolution) and broad spatial coverage; SBAS is designed to maximize the number of coherent points over large areas, isolate high frequency components by subtracting the regional mean signal, and employ mathematical tools (e.g., SVD) to solve systems that include subsets separated by large baselines [26].

SqueeSARTM extends the PS approach by combining point like PS and Distributed Scatterers (DS), areas with spatially coherent but non dominant radar response, offering both a largely automated Standard mode and an expert driven Advanced mode to maximize usable measurement points; by incorporating DS analysis, SqueeSAR increases point density in partially urbanized or sparsely vegetated areas, making it well suited to mixed urban–rural scenarios while maintaining precision comparable to PS methods but with greater spatial coverage.

StaMPS merges PS and SB criteria, selecting stable pixels through amplitude analysis and spatial correlation to operate in non urban areas and under non stationary deformation regimes; TomoSAR exploits multi angle acquisitions to reconstruct the vertical distribution of scatterers and boost information density in complex scenes.

These methodologies are often combined in hybrid or multi scale workflows to balance precision, spatial density and robustness to decorrelation across diverse application contexts (urban, rural, volcanic, seismic) [5].

3 | InSAR data Processing and Methodology

Interferometric deformation data can be represented in different ways depending on the processing technique adopted. In PSI, results are typically expressed as PSs, i.e. radar targets whose electromagnetic response remains stable over time. These points often correspond to building façades, metal elements, or other natural and artificial reflectors. The density of PS varies with wavelength and acquisition geometry: C-band missions commonly provide on the order of 100 to 400 points/km^2, while X-band systems can reach several thousand points/km^2. For each PS, the position, mean displacement rate and full displacement time series are available, allowing detailed point-wise analyzes [5].

Other interferometric approaches, such as SBAS or Distributed Scatterer (DS) techniques, produce deformation information in different formats, often with lower point density but broader spatial coverage. Regardless of the specific representation, assessing the condition of civil structures requires integrating information from multiple radar targets, since buildings and infrastructures exhibit complex geometries and heterogeneous materials that make the kinematics of individual components difficult to interpret in isolation. Aggregating data from many PS or DS points reduces uncertainty and supports structural and geotechnical evaluations.

First, the chapter presents the analysis based on a single dataset (ascending or descending) and its inherent limitations. It then addresses the combination of measurements from both datasets to retrieve the vertical and horizontal displacement components, and finally illustrates how the global reference frame can be rotated to define local reference systems, enabling the decomposition of motion into longitudinal, transverse, and vertical displacements. Since PSs from different datasets rarely coincide, spatial and/or temporal resampling (interpolation or subsampling) is often necessary to obtain comparable values at the same locations.

Finally, the choice of processing method and the achievable information level depend strongly on the structure type and orientation (for example, an E–W versus N–S oriented structure can yield different deformation insights), as well as on the quantity and quality of the datasets. The chapter closes with considerations on 3D interpolation possibilities and a critical assessment of method performance, limitations, and practical cautions for a rational application of interferometric satellite data to geotechnical and structural problems.

3.1. Use of a Single-Orbit Dataset Methodology

The analysis of data derived from the processing of a single satellite orbit (either ascending or descending) can offer an initial overview of ongoing deformation processes. Nevertheless, deformation information extracted from a single dataset has intrinsic limitations, as it provides displacement and mean velocity only along the LOS direction. This means that the full three-dimensional displacement field cannot be uniquely reconstructed from a single viewing geometry.

The proportion of actual ground displacement that can be detected through satellite observations depends both on the true displacement direction and on the incidence angle between the LOS and the Earth's surface. As discussed in Chapter 2, this angle is determined by the orbit inclination angle ϕ (heading angle) and the look angle θ (off-nadir), as illustrated in Figure 2.3. It is worth noting that, even for the same satellite and acquisition mode, these angles may vary slightly from pixel to pixel within the same scene.

Regarding the generalized deformation measurement (d_{LOS}), which may represent either displacement or average displacement velocity, the value observed along the ascending and descending LOS (A/D) can be expressed as a linear combination of the displacement components along the three principal directions: East–West (d_E), North–South (d_N), and vertical (d_U):

$$\begin{cases} d_{LOS,A} = d_E \cdot cos(\alpha_{E,A}) + d_N \cdot cos(\alpha_{N,A}) + d_U \cdot cos(\alpha_{U,A}) \\ d_{LOS,D} = d_E \cdot cos(\alpha_{E,D}) + d_N \cdot cos(\alpha_{N,D}) + d_U \cdot cos(\alpha_{U,D}) \end{cases} \tag{6}$$

In this formulation, the terms $cos(\alpha_E)$, $cos(\alpha_N)$, $cos(\alpha_U)$, denote the direction cosines of the angles (α_E), (α_N), and (α_U), which relate the E–W, N–S, and vertical axes to the LOS (A/D), respectively. These cosines correspond to the components of the unit vectors defining the ascending and descending LOS directions, represented by the symbols:

$$\begin{cases} cos(\alpha_{E,A/D}) = sin(\theta_{E,A}) \cdot cos(\phi_{A,D}) \\ cos(\alpha_{N,A/D}) = sin(\theta_{E,A}) \cdot sin(\phi_{A,D}) \\ cos(\alpha_{U,A/D}) = cos(\theta_{A,D}) \end{cases} \tag{7}$$

Equations 6 highlights that the fraction of displacement (or average displacement velocity) detectable along the LOS depends directly on the values of these direction cosines.

As an extreme case, when the true displacement direction is perpendicular to the LOS, the sensor records no measurable component. Consequently, a significant LOS displacement is a clear indicator of an active deformation process, whereas a small LOS displacement does not

necessarily imply the absence of ground movement. By convention, positive values indicate motion toward the satellite, while negative values correspond to motion away from it.
It is important to recall that the spatial distribution of measurement points is inherently non-uniform. To support the interpretation of deformation patterns and extend displacement information to areas lacking radar targets, point measurements can be interpolated using spatial interpolation algorithms, either deterministic or geostatistical [5], [27].

3.2. Use of Dual-Orbit Datasets Methodology

Using both viewing geometries produces a more complete three dimensional representation of the monitored terrain or structure because each orbit supplies complementary perspectives.
Even a direct comparison of LOS displacement components from the two geometries can be highly informative for deformation analysis. For example, for a displacement whose true horizontal velocity lies along the east–west axis (see Figure 3.1) and assuming identical incidence angles, the LOS measurements from ascending and descending passes will have the same magnitude but opposite signs. This occurs because the satellites travel in opposite directions: the same horizontal motion appears as either a movement away from the sensor (negative) or toward the sensor (positive).

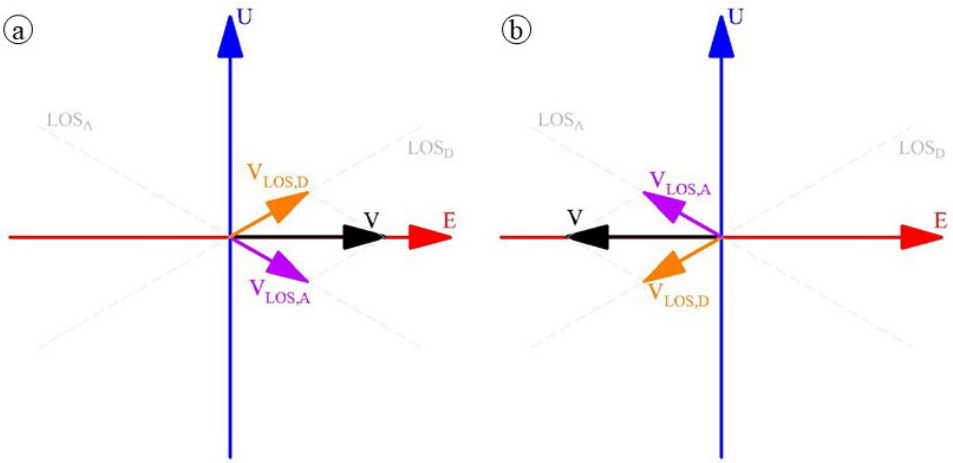

Figure 3.1: Example of decomposition of a horizontal velocity vector on the E-U plane. (a) Displacement towards the descending orbit; (b) Displacement towards the ascending orbit [27].

In contrast, for a displacement with a true vertical velocity component (see Figure 3.2) and equal incidence angles, the LOS magnitudes measured in both orbits coincide and their signs agree: negative values indicate subsidence (motion away from the satellite), while positive values indicate uplift (motion toward the satellite) [27]. The common approach is to combine

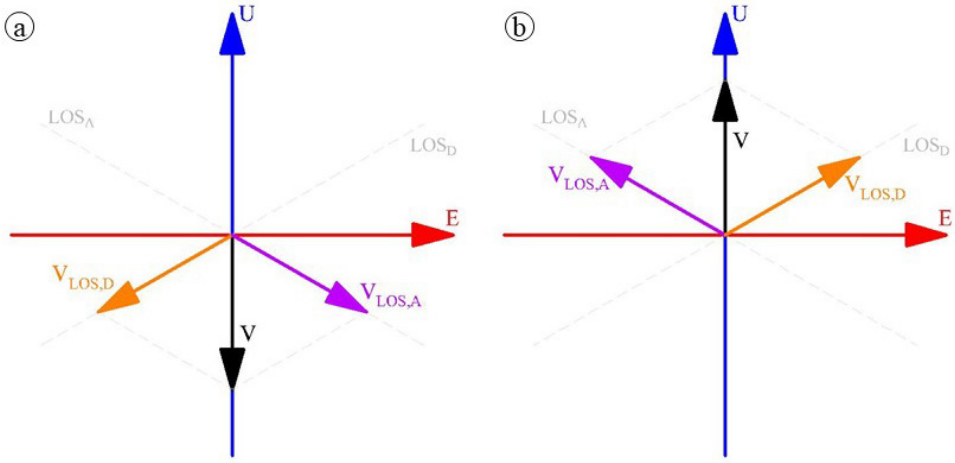

Figure 3.2: Example of decomposition of a vertical velocity vector on the E-U plane (a) Displacement towards the satellite;(b) Displacement away from the satellite [27].

ascending and descending observations to resolve the vertical and horizontal components of the velocity vector in the E–U plane. This decomposition provides a better characterization of deformation processes and supports the detection of structural anomalies.
It should be noted that it is uncommon for the same PS to be observed in both acquisition geometries, since such points are typically artificial reflectors or targets equally visible from both directions. Consequently, spatial and temporal resampling is usually required to produce consistent paired datasets.
According to the following Reference [28], the reconstruction of structural displacement of a linear structure using satellite observations from two distinct orbits comprises the following principal steps: Selection and clustering of PSs, Rotation of the reference system, Baseline removal and computation of mean displacement, Temporal Resampling and Combination of ascending and descending data:

- *Selection and clustering of PSs:* The initial phase involves selecting the PSs relevant to the structure. The analysed structure is subdivided into predefined zones corresponding to specific areas or elements of interest, and all PSs falling within each zone are grouped together to form distinct clusters. For each cluster, an average displacement time series is computed from the PSs it contains, providing a representative signal for that portion of the structure.

- *Rotation of the reference system:* Using the (E, N, U) reference system previously introduced, a generic displacement vector d and the unit vector u_{LOS} associated with the LOS

can be expressed through the following relationships:

$$\mathbf{d} = \begin{bmatrix} d_E \\ d_N \\ d_U \end{bmatrix} \tag{8}$$

$$\mathbf{u}_{LOS} = \begin{bmatrix} cos\alpha_E \\ cos\alpha_N \\ cos\alpha_U \end{bmatrix} \tag{9}$$

where the terms $cos\alpha_E, cos\alpha_N, cos\alpha_U$ are the direction cosines of the LOS direction; $\alpha_E, \alpha_N, \alpha_U$ are the angles subtended by the LOS direction with the E, N, and U axes; d_E, d_N, d_U are three orthogonal components of the displacement vector, as illustrated in Figure 3.3.

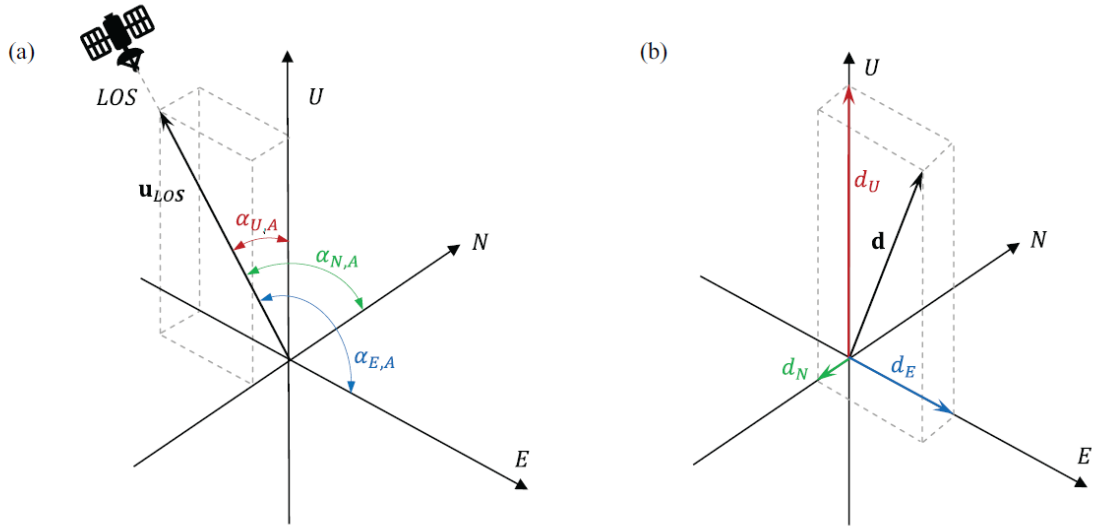

Figure 3.3: Representation of (a) the unit vector u_{LOS} associated with the LOS direction and the (E, N, and U) reference system, (b) displacement vector d along with its components in the E, N and U directions [29].

Another way to express the d and u_{LOS} is in spherical coordinates within the (E, N, and U) space, as shown in Figure 3.4. This vectors are defined as it follows:

$$\mathbf{d} = d \cdot \begin{bmatrix} sin(\omega)cos\varphi \\ -sin(\omega)sin\varphi \\ cos\omega \end{bmatrix} \tag{10}$$

$$\mathbf{u}_{LOS} = \begin{bmatrix} sin(\alpha_U)cos\alpha_{ALD} \\ -sin(\alpha_U)sin\alpha_{ALD} \\ cos\alpha_U \end{bmatrix} \tag{11}$$

where d is the magnitude of **d**, ω is the angle between the direction of the vector d and the vertical, φ is the angle between the Azimuth Looking Direction (ALD) and the E direction. These relationships are valid for structures with a longitudinal axis aligned with the E direction in the E-N plane. Both representations are useful for projecting LOS measurements onto local displacement components; by combining the two formulations for u_{LOS} (9 and 11), the angle of the Azimuth Looking Direction α_{ALD} can be derived for each orbit (ascending and descending). However, for a generic structural element whose longitudinal axis forms an angle with the E direction, it is useful to introduce a new coordinate system (L, T, U). In this system, the L-axis represents the longitudinal direction of the structure, the T-axis is the transverse direction, perpendicular to L in the E-N plane, and the U-axis coincides with the vertical direction.

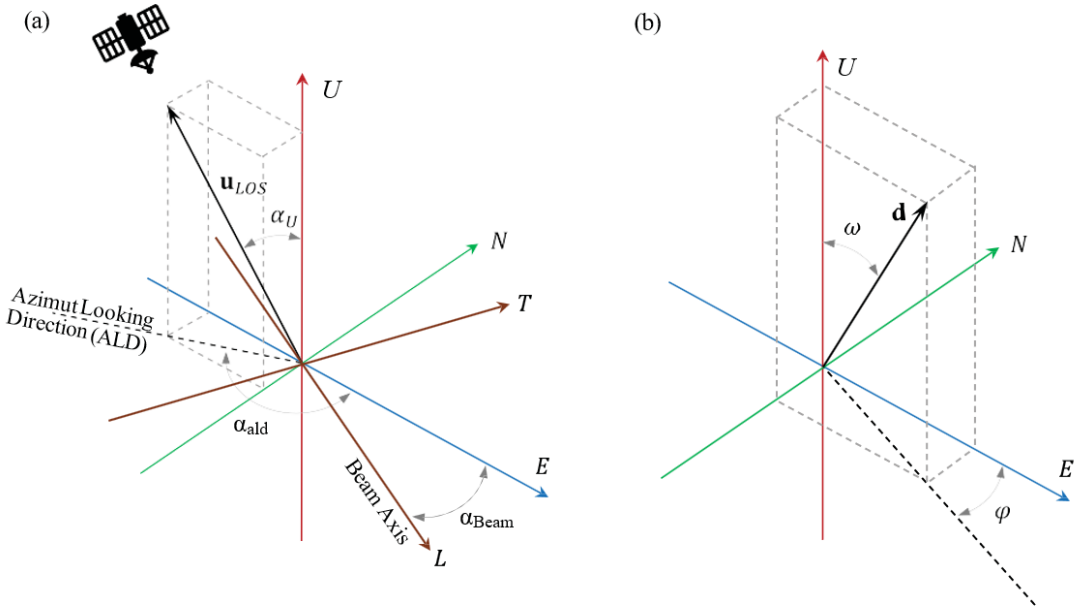

Figure 3.4: Representation of (a) the unit vector u_{LOS} associated with the LOS direction and the (L, T, and U) reference system, (b) definition of angles ω and φ [29].

Adopting this reference system, aligned with the actual orientation of the structure, simplifies the formulation of the displacement components, eliminating the trigonometric terms that describe the rotation relative to the axes.

The new reference system is obtained by rotating the original coordinate frame by an angle α_{Beam} around the U-axis, which represents the clockwise rotation from the East

direction to the structure's axis, as measured on the planimetry. It therefore defines the local longitudinal direction of the structure and determines how the global displacement components must be transformed to analyse deformation along that specific structural element. The rotation is described by the following rotation matrix R_U:

$$\mathbf{R}_U = \begin{bmatrix} cos\alpha_{Beam} & -sin\alpha_{Beam} & 0 \\ sin\alpha_{Beam} & cos\alpha_{Beam} & 0 \\ 0 & 0 & 1 \end{bmatrix} \tag{12}$$

Once the rotation matrix is introduced, the components of the vectors $\mathbf{d}$ and $\mathbf{u}_{LOS}$ in the new reference system (L, T, U) can be expressed as follows:

$$\mathbf{d'} = \mathbf{R}_U \times \mathbf{d} = \begin{bmatrix} sin(\omega)cos(\varphi - \alpha_{Beam}) \\ -sin(\omega)sin(\alpha_{Beam} - \varphi \\ cos\omega \end{bmatrix} \tag{13}$$

$$\mathbf{u'}_{LOS} = \mathbf{R}_U \times \mathbf{u}_{LOS} = \begin{bmatrix} sin(\alpha_U)cos(\alpha_{ALD} - \alpha_{Beam}) \\ -sin(\alpha_U)sin(\alpha_{ALD} - \alpha_{Beam}) \\ cos\alpha_U \end{bmatrix} \tag{14}$$

The projection of the displacement along the LOS, d_{LOS}, can then be expressed as the scalar product of the determined vectors:

$$\begin{aligned} d_{LOS} = \mathbf{d'} \cdot \mathbf{u'}_{LOS} = &+ d\, sin\omega\, cos(\alpha_{Beam} - \varphi)\, sin\alpha_U\, cos(\alpha_{ALD} - \alpha_{Beam}) \\ &- d\, sin\omega\, sin(\alpha_{Beam} - \varphi)\, sin\alpha_U\, sin(\alpha_{ALD} - \alpha_{Beam}) \\ &+ d\, cos\omega\, cos\alpha_U \end{aligned} \tag{15}$$

Since the displacement along the LOS can be seen as a linear combination of the displacement components along the main longitudinal, d_L, transverse, d_T, and vertical, d_U, directions, these components can be expressed in terms of the angles ω, φ, and α_{Beam} through the following relationships:

$$d_L = d\, sin\omega\, cos(\alpha_{Beam} - \varphi) \tag{16}$$

$$d_T = d\, sin\omega\, sin(\alpha_{Beam} - \varphi) \tag{17}$$

$$d_U = d\, cos\omega \tag{18}$$

Substituting these expressions into the equation for d_{LOS} yields:

$$d_{LOS} = d_L\, sin\alpha_U\, cos(\alpha_{ALD} - \alpha_{Beam}) - d_T\, sin\alpha_U\, sin(\alpha_{ALD} - \alpha_{Beam}) + d_U\, cos\alpha_U \quad (19)$$

- *Baseline Removal and computation of mean displacements:* The initial velocity value in each time series is removed by subtracting it from all subsequent measurements. This normalization step aligns the series to a shared baseline, eliminating early offsets or noise that might otherwise influence the interpretation. After this correction, at each time step, the mean value of the dislpacement of all PSs within the selected area is computed to produce a mean-displacement time series.

- *Temporal Resampling:* Temporal resampling is applied to the ascending and descending datasets, necessary because acquisitions likely occur on different days for the two orbits. Specifically, their mean time series are temporally aligned by interpolation to produce a consistent set of observations across the full acquisition timeline; linear interpolation is adopted for this purpose.

- *Combination of Ascending and Descending Data:* Given the vectors $d_{LOS,A}$ and $d_{LOS,D}$ measured along LOS_A and LOS_D, equation 19 can be cast into the following linear system:

$$\begin{cases} d_{LOS,A} = d_L\, \sin\alpha_{U,A}\, \cos(\alpha_{ALD,A} - \alpha_{Beam}) - d_T\, \sin\alpha_{U,A}\, \sin(\alpha_{ALD,A} - \alpha_{Beam}) \\ \qquad\qquad + d_U\, \cos\alpha_{U,A} \\ d_{LOS,D} = d_L\, \sin\alpha_{U,D}\, \cos(\alpha_{ALD,D} - \alpha_{Beam}) - d_T\, \sin\alpha_{U,D}\, \sin(\alpha_{ALD,D} - \alpha_{Beam}) \\ \qquad\qquad + d_U\, \cos\alpha_{U,D} \end{cases} \quad (20)$$

The system contains three unknowns (d_L, d_T, d_U) but only two independent equations, making it underdetermined. To obtain a solution, it is necessary to introduce an assumption that reduces the number of unknowns from three to two, typically by prescribing the plane of motion. In the case of linear structure, often the transversal displacements are neglected.

These considerations form the basis of the method adopted in this chapter, which focuses on estimating the longitudinal and vertical components of the true deformation vector. Once system (20) is formulated using the satellite direction cosines for each acquisition geometry, imposing the condition $d_T = 0$ reduces the problem to a system of two equations

with two unknowns:

$$\begin{cases} d_{LOS,A} = d_L \cdot sin\alpha_{U,A}\, cos(\alpha_{ald,A} - \alpha_{Beam}) + d_U \cdot cos\alpha_{U,A} \\ d_{LOS,D} = d_L \cdot sin\alpha_{U,D}\, cos(\alpha_{ald,D} - \alpha_{Beam}) + d_U \cdot cos\alpha_{U,D} \end{cases} \tag{21}$$

Intoducing:

$$\begin{cases} a_A = sin\alpha_{U,A}\, cos(\alpha_{ald,A} - \alpha_{Beam}) \\ b_A = cos\alpha_{U,A} \\ a_D = sin\alpha_{U,D}\, cos(\alpha_{ald,D} - \alpha_{Beam}) \\ b_D = cos\alpha_{U,D} \end{cases} \tag{22}$$

The system becomes:

$$\begin{cases} d_{LOS,A} = a_A \cdot d_L + b_A \cdot d_U \\ d_{LOS,D} = a_D \cdot d_L + b_D \cdot d_U \end{cases} \tag{23}$$

And the longitudinal and vertical components are:

$$\begin{cases} d_L = \dfrac{d_{LOS,A} \cdot b_D - d_{LOS,D} \cdot b_A}{a_A \cdot b_D - a_D \cdot b_A} \\ d_U = \dfrac{d_{LOS,D} \cdot a_A - d_{LOS,D} \cdot a_D}{a_A \cdot b_D - a_D \cdot b_A} \end{cases} \tag{24}$$

3.3. Regional subsidence modelling and removal

Displacement time series derived from InSAR measurements can exhibit a homogeneous temporal behaviour across neighbouring measurement points due to general ground movements. This effect typically reflects the presence of a large-scale deformation component that dominates the observed signal. When this trend is present, it can mask the local variations that are relevant for assessing the structural response of individual buildings or infrastructure elements. For this reason, separating the regional deformation from the local behaviour is a necessary step before any structural interpretation can be carried out.

An important step is the identification of PSs that reliably represent the large-scale ground motion. To avoid introducing subjectivity into the analysis, all points located in the surroundings of the structure are included, ensuring that no potentially informative measurements are discarded on the basis of arbitrary choices.

The regional trend is estimated separately for the two LOS geometries, after which the corresponding trend from each method is removed from the displacement time series of the structure. The resulting detrended data isolate the local deformation behaviour and form the basis for the structural analysis. This transition marks the shift from large-scale geophysical modelling to the detailed investigation of the structure's response.

Two approaches are introduced to estimate this regional trend:

- *Method 1, Removal of soil Mean Displacement:* The first method estimates the regional deformation by computing the mean displacement of the PSs located in the area surrounding the structure. The assumption is that these points are mainly affected by a common large-scale ground motion, while deviations from this trend may reflect local behaviour.

  For each acquisition date, the LOS displacements of the selected PSs are averaged to obtain a representative regional value. Repeating this operation over the full time span yields a mean displacement time series describing the large-scale component. This series is subtracted from the LOS displacement of the structure before reconstructing the vertical and longitudinal displacement components, so that the derived quantities are referred to a corrected signal in which the regional trend has been removed.

  The definition of the reference area is a critical aspect of the method. Its spatial extent is not straightforward to determine, and different choices may lead to different regional trends and, consequently, different residual structural displacements. The selected area should therefore be sufficiently representative of the regional ground behaviour while remaining independent from local structural effects.

- *Method 2, Use of Parametric Curve Fitting:* In this method, the regional deformation is estimated by fitting a polynomial function to the displacement time histories of the PSs located around the structure. Unlike the simple mean-based approach, the fitted function provides a smoother representation of the common temporal evolution of ground motion. The displacement series of the surrounding PSs are considered together to identify a single time-dependent trend representative of the large-scale deformation affecting the area. The resulting polynomial function describes the regional component of motion and is evaluated at each acquisition epoch. This estimated trend is then subtracted from the LOS displacement of the structural points before reconstructing the vertical and longitudinal components.

  To assess the adequacy of the fitted model, the coefficient of determination R^2 is evaluated, quantifying the proportion of variance in the displacement time series that is explained by the polynomial function: values close to 1 indicate that the model captures the common temporal trend, whereas lower values suggest that the chosen degree may be insufficient or that the data contain significant local variability.

  By relying on a continuous parametric function, this approach reduces short-term fluctuations and measurement noise, providing a more stable estimate of the background deformation. However, the choice of the polynomial degree influences the smoothness of the estimated trend and may affect the residual structural displacement. For this reason, the model must remain sufficiently simple to capture the regional behaviour without introducing artificial features.

4 | Case Study: Roof Structure of the Diego Armando Maradona Stadium

The Diego Armando Maradona Stadium represents a relevant case study for the application of InSAR-based structural deformation analysis. Its large size, open surroundings, and clear visibility from space make it particularly suitable for satellite observations, while the absence of adjacent tall buildings reduces geometric distortions and facilitates the interpretation of LOS displacements.

From a structural perspective, the stadium offers an additional element of interest: its roof system is composed of repeated structural modules arranged along an elliptical plan, resulting in locally varying orientations of the structural axes. This configuration provides an opportunity to assess the capability of InSAR techniques to capture deformation patterns in a multidirectional system, extending their use beyond the more common linear infrastructures with a single dominant longitudinal direction.

Figure 4.1: Diego Armando Maradona Stadium [30].

The choice of this case study is further motivated by the stadium's location within the Campi

Flegrei caldera, an active volcanic area affected by ground deformation phenomena. These geodynamic processes may influence the behaviour of the roof structure over time, making continuous monitoring particularly relevant for understanding potential long term effects on the stadium's integrity.
The satellite data used in this study were acquired by the COSMO SkyMed constellation, that provides high resolution SAR data. The analysis focuses on characterising the deformation behaviour of the stadium roof and on determining whether local structural responses can be distinguished from the large-scale ground motion affecting the surrounding area. The roof's modular configuration, arranged along an elliptical plan with varying orientations, provides an opportunity to examine how InSAR measurements capture deformation patterns in a multidirectional structural system.
To facilitate the interpretation of the results, this chapter presents the displacement components derived from the InSAR processing workflow described in Chapter 3 and subsequently refined through the regional-trend removal methods. The combination of these steps enables a clear separation between large-scale ground motion and the local behaviour of the roof, allowing the deformation patterns of the structure to be examined in detail in the following sections.

4.1. Case Study description

The stadium was constructed between 1952 and 1959, based on a design by architect Carlo Cocchia. A comprehensive renovation was undertaken in 1990 by Fabrizio Cocchia, Giuseppe Squillante, and Luigi Corradi. The works included the construction of the roof and the new press stand, both developed according to Corradi's structural design, the installation of two elevators providing access to the press area, and the addition of an elevated structure above the main stand, known as the "Dirigibile", intended to accommodate commentators and television production units [31].
Further interventions involved the refurbishment of the building adjacent to the main stand, the installation of individual seating throughout the stadium, the modernization of the athletics track and lighting system, the replacement of the original scoreboard with two displays mounted on the balustrade, the redesign of the entrance areas, the construction of an underground multi storey car park, and compliance upgrades to meet FIFA safety standards. For the 1990 World Cup, a third tier was added.
Between 1990 and 2010, the facility experienced progressive structural deterioration. The first issues emerged in 1995, and a severe storm in 2001 exposed both the inadequacy of the drainage system and a structural vulnerability: located at the lowest point of Fuorigrotta, the stadium collects runoff from the Monte Sant'Angelo hillside. During this period, the third tier was also closed, as the vibrations generated by spectators' celebrations propagated through the roof

supporting pylons into the surrounding buildings [32], [33].
In 2008, maintenance work was carried out on the roof. The project itself had originally won the CONI competition in 1948, despite initial controversy regarding the proposed site. Once the current location was approved, construction proceeded and culminated in the stadium's inauguration in 1959. Designed to accommodate 60,000 spectators, the structure consists of two rings separated by a wide horizontal gap: the lower ring is built directly on the ground, while the upper ring rests on fifty six reinforced concrete ribs inclined downward from top to bottom.
The structural system is composed of reinforced concrete, with façade materials including reinforced concrete, brick cladding, metal structures, and plastic components. The roof is a flat assembly of steel and polycarbonate as shown in Figure 4.2 [34].

Figure 4.2: Diego Armando Maradona Stadium Roof [34].

The roof structure of the Diego Armando Maradona Stadium is composed of a series of steel truss beams arranged radially along the upper perimeter of the facility. These structural elements, referred to as "decks," consist of 28 units evenly distributed along the outer ring of the grandstand. Among them, 16 support the stadium's lighting system, with the luminaires mounted on dedicated secondary steel frames (see Figure 4.3) [35].
Each deck is a triangular-pattern steel truss with a free span of 41.65 m, as indicated in the preliminary design documentation [36]. The trusses are supported by steel columns positioned along the external perimeter of the grandstand.

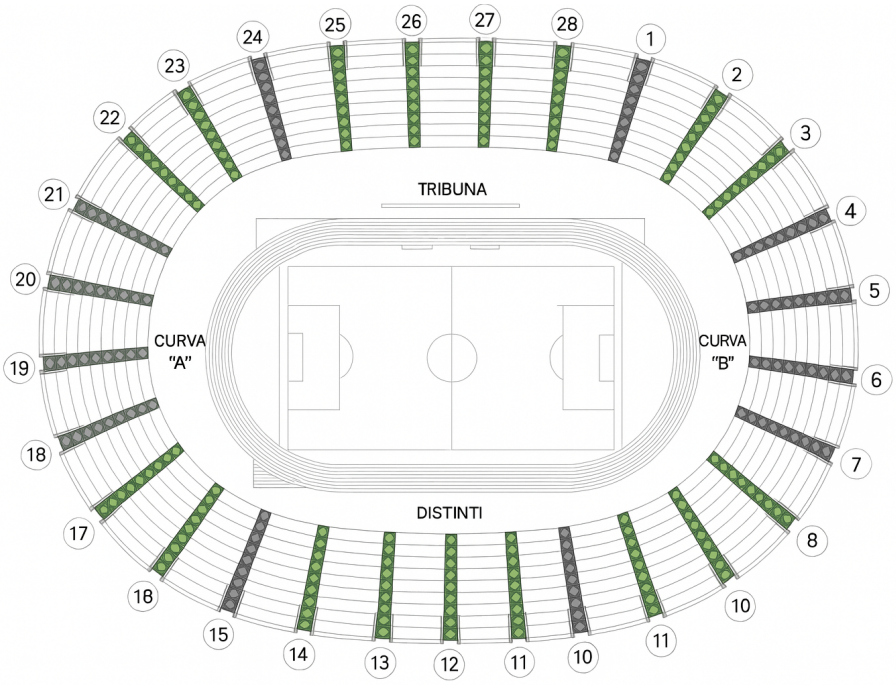

Figure 4.3: Plan of the stadium showing deck numbering. Decks currently equipped with floodlights are highlighted in green [37].

To analyse the structural behaviour of the roof, the entire system was first subdivided into 28 sectors, each corresponding to one of the radial truss beams ("decks"). This approach made it possible to evaluate the displacements as a function of the varying angle between each truss and the East direction, using a dedicated local reference system for every zone.
Each of the 28 zones was then further divided into two sub-regions: the portion adjacent to the supporting columns, and the portion extending towards the pitch, the latter being potentially more sensitive to structural deformations, as shown in Figure 4.4.
As a first modelling assumption, each truss was idealised as a cantilever beam fixed at the column, allowing an initial assessment of its deformation behaviour. This simplification was adopted with the awareness that the real structure exhibits a global, interconnected response, since all trusses are linked through the elliptical ring of the roof, which provides additional stiffness and constraint continuity.

Figure 4.4: Subdivision of the Roof in 28 zones extending towards the city (a) and towards the pitch (b).

4.2. InSAR data processing

The interferometric products used in this study were generated by CNR IREA using the P-SBAS (Parallel SBAS) processing chain, based on COSMO-SkyMed (CSK) SAR imagery acquired in Stripmap mode. The datasets cover a time span from July 2009 to March 2025, with a total of 432 acquisition dates, and were processed using the SRTM 1 arcsec DEM within the WGS84 geographic reference system (EPSG:4326). The Stripmap acquisition mode provides a ground resolution of approximately 3 $\times$ 3 m, suitable for detailed deformation analysis over urban structures. Since Stripmap products have a relatively narrow swath, only the CSK tracks whose footprint intersects the area surrounding the Diego Armando Maradona Stadium were selected. This resulted in the use of distinct ascending and descending datasets, each providing

a separate set of PSs for analysing the deformation behaviour around the stadium.
Starting from the full footprints of the selected ascending and descending tracks, a spatial subset was extracted by defining a square area of approximately 1 km^2 centered on the stadium. This spatial window was chosen as a compromise between the need to capture the regional deformation pattern and the requirement to focus on the structural response of the stadium and its immediate surroundings. In a subsequent step, MPs located directly on the stadium structure were isolated from those belonging to the surrounding urban environment, allowing the analysis to distinguish regional ground deformation from local structural behaviour.
The COSMO-SkyMed P-SBAS datasets provide a set of PSs distributed across the area of interest, each associated with a time series of displacement measured along the LOS. For every PS, the dataset includes:

- Geographic coordinates (latitude, longitude) in EPSG:4326
- Elevation derived from the SRTM 1 arcsec DEM
- LOS displacement time series (in meters)
- Mean LOS velocity (in cm/yr)
- Temporal sampling corresponding to the 432 acquisition dates
- Metadata describing acquisition geometry (ascending or descending orbit)

LOS displacements positive values indicate movement towards the satellite, while negative values indicate movement away from it. Since ascending and descending geometries observe the same area from different look angles, the two datasets provide complementary sensitivity to vertical and horizontal components of deformation.
Figure 4.5 summarises the resulting spatial distribution: panels (a) and (b) show the PS within the 1 km^2 area around the stadium, while panels (c) and (d) focus on the PSs located on the stadium roof. The points are coloured according to the average displacement velocity along the LOS computed over the entire observation period. The colour scale spans -13 to +13 mm/yr and is centred on zero, with positive values indicating motion toward the satellite and negative values indicating motion away from it. Roof points exhibit a mean LOS velocity of approximately -6.5 mm/yr in ascending geometry and +11 mm/yr in descending geometry.

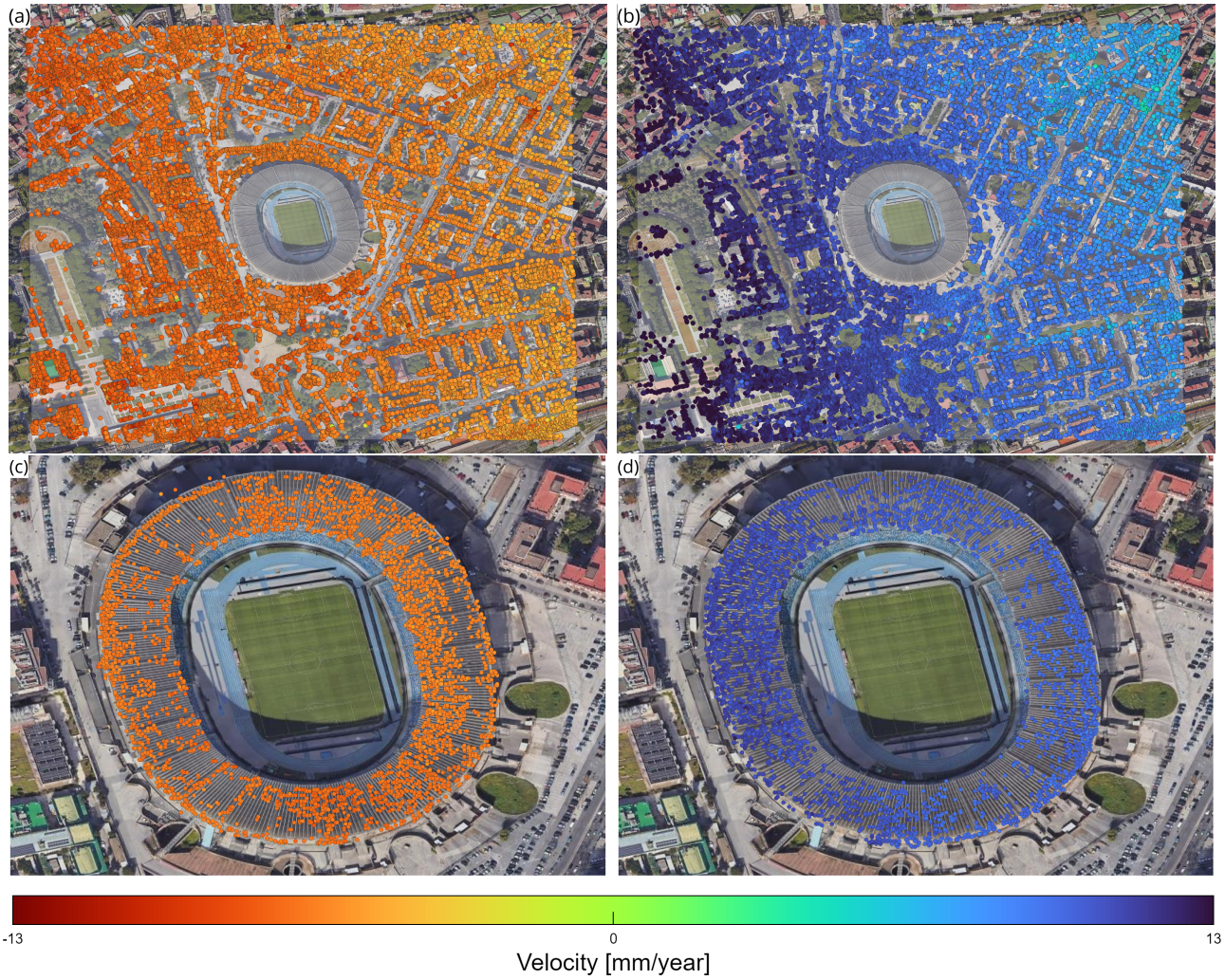

Figure 4.5: Distribution of selected persistent scatterer (PS) points within a 1 km^2 area around the stadium and separately on the stadium roof, shown for ascending (a) and (c) and descending (b) and (d) acquisitions.

To assess the internal consistency of the COSMO SkyMed PSs and to verify whether the deformation signals recorded on the stadium exhibit coherent temporal behaviour, a correlation analysis was performed using the Pearson Correlation Coefficient (PCC). For each pair of PSs, the PCC quantifies the degree of linear similarity between their LOS displacement time series, with values ranging from:

- +1 → perfect positive linear correlation;
- 0 → absence of correlation;
- -1 → perfect negative linear correlation.

This metric provides a robust and intuitive way to evaluate whether PSs share a common deformation trend or whether some points behave anomalously.

For each area and for both the ascending and descending datasets, a full correlation matrix was computed, containing the PCC values for all possible pairs of PSs. These matrices were then visualised as colour coded heatmaps, allowing an immediate qualitative assessment of the correlation structure across the area. Figure 4.6 shows the correlation matrix for 4 selected zones.

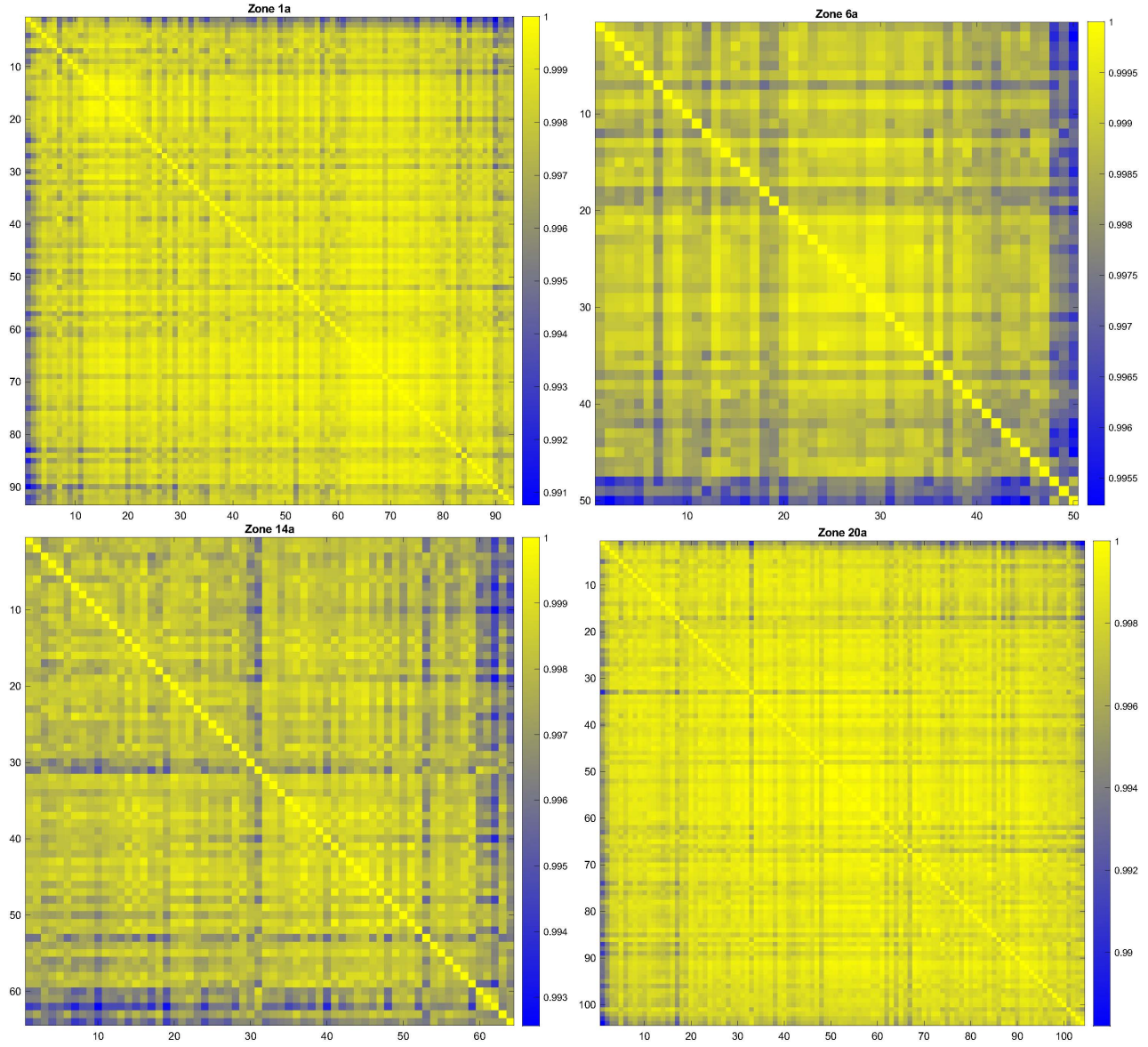

Figure 4.6: PCC matrix for ascending PSs in zones 1a, 6a, 14a and 20a.

The matrices display a high degree of internal consistency: within each zone, most PSs exhibit strong positive correlations with one another, confirming that the deformation signal is highly coherent at the local scale and dominated by a common temporal trend. Even the minimum Pearson coefficient within each zone remains above 0.9, indicating an excellent level of similarity

among the PSs belonging to the same structural area. This internal coherence is consistently observed across the entire roof.

Before proceeding with the deformation analysis, a series of preprocessing steps and quality controls were carried out to ensure the reliability of the PSs, by identifying potential outliers and removing points affected by anomalous displacement time series.

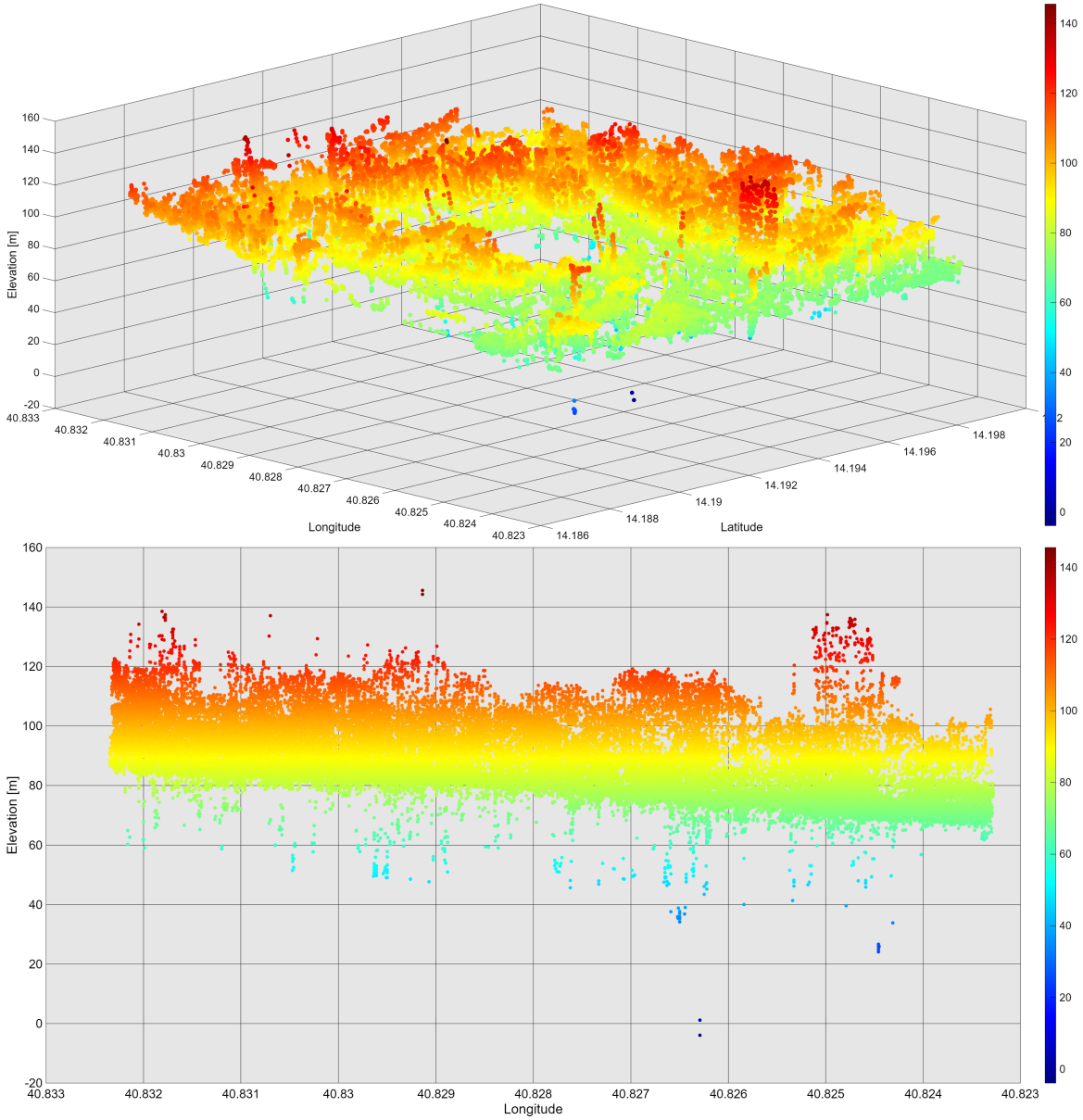

Figure 4.7: 3D and 2D plotter for ascending regional PS within a 1 km^2 area around the stadium.

The first inspection focused on the geometric consistency of the PSs within the selected 1 km^2 area surrounding the stadium. To this end, all points were visualized in a three dimensional MATLAB environment, using their planimetric coordinates and elevation values. The 3D representation allowed an assessment of the spatial distribution of the PSs and facilitated the

identification of altimetric outliers, i.e., points exhibiting unrealistic elevation values that were clearly inconsistent with the surrounding topography (see Figure 4.7).
These anomalous points are typically associated with satellite geolocation uncertainties, DEM inaccuracies, or local phase unwrapping artefacts.
To assess the nature and impact of potential outliers, the elevation distribution was first modelled as a Gaussian curve (Figure 4.8). By comparing this distribution with the 3D plot of the area, it becomes evident that the lower outliers cluster around 60 m and the upper ones around 120 m. Defining the 1st and 99th percentiles naturally isolates these same ranges.

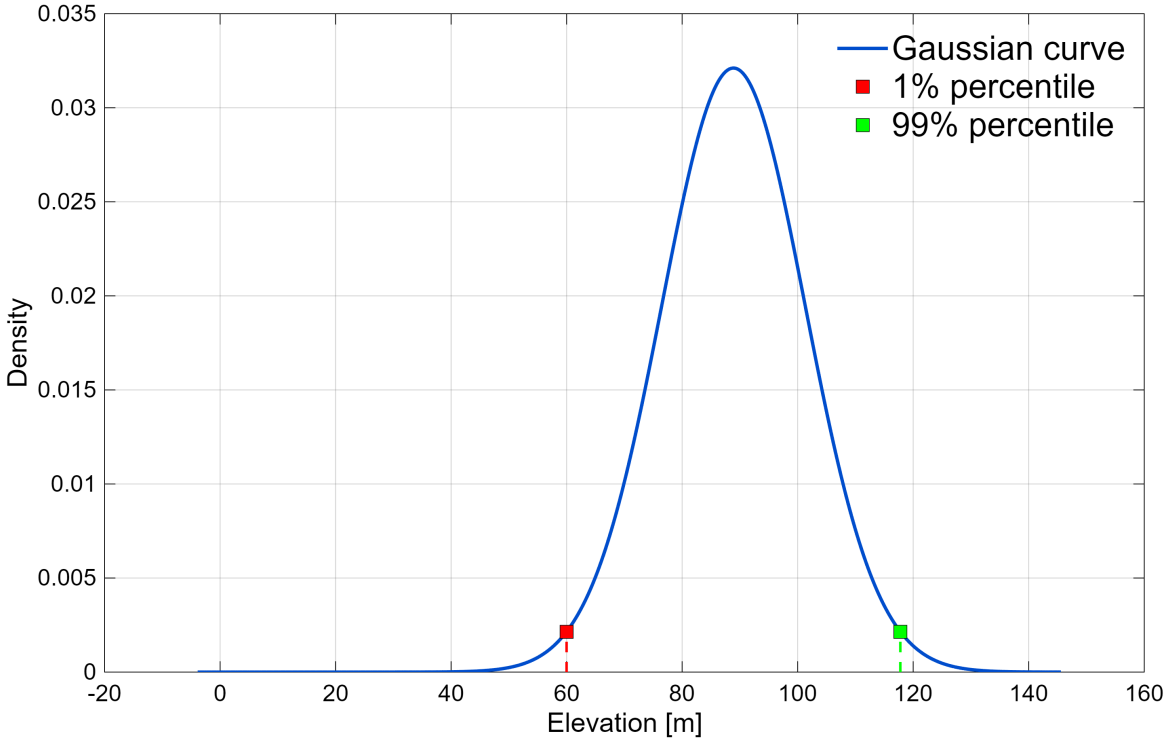

Figure 4.8: Gaussian curve with 1st and 99th percentiles for ascending data.

Points with elevations below the 1% threshold and above the 99% threshold were therefore identified and temporarily discarded. The mean displacement time series was then computed both with and without these points, and the two resulting curves exhibit a similar temporal behaviour (see Figure 4.9). This confirms that the extreme elevation values reflect only altimetric inaccuracies rather than anomalies in the deformation signal. For this reason, these points are retained in the subsequent analyses, as they contribute additional observations without introducing spurious temporal effects.

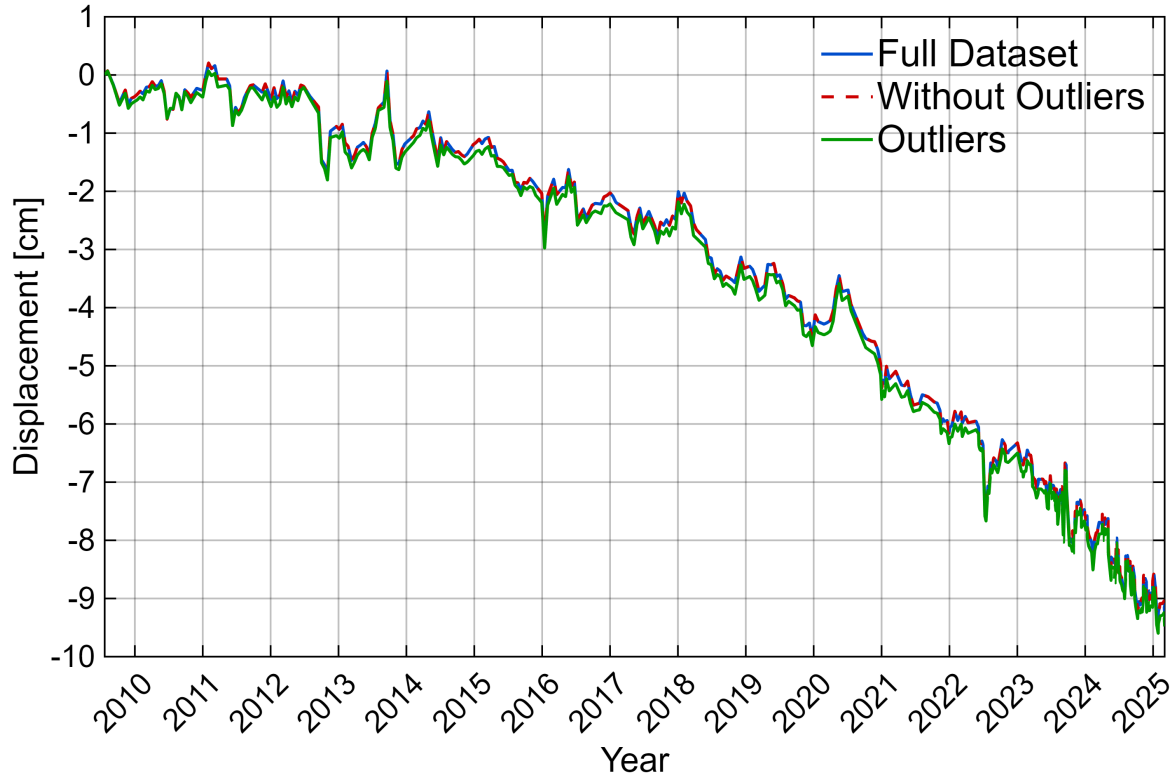

Figure 4.9: Mean displacement time series for ascending dataset: Full Dataset (blue), Without Outliers (red) and Outliers (green).

After this preliminary screening, the PSs were divided into two categories:

- Regional, located in the urban environment surrounding the stadium;
- Structural, located directly on the stadium roof and stands.

The regional PSs are used to estimate and remove the large scale background deformation affecting the entire area, while the structural PSs are used to characterise the local behaviour of the stadium. Building on the structural subdivision already introduced in the case study description, the results of the correlation analysis confirm that the COSMO-SkyMed measurement points behave coherently within the surrounding area.
The next section examines how regional ground motion can be separated from local structural behaviour in a reliable and interpretable way.

4.3. Regional subsidence modelling and removal

The displacement time series extracted around the stadium show a largely homogeneous temporal behaviour, reflecting the regional subsidence affecting Naples and the Campi Flegrei area. This broad, spatially coherent deformation component dominates the LOS measurements and causes individual PSs to display similar trends, making it difficult to distinguish the specific response of the roof from the surrounding ground motion. For the purposes of this case study, separating the regional contribution from the local structural behaviour is therefore a necessary step. To estimate the regional component, all PSs located within a 1 km^2 area surrounding the stadium were used, explicitly excluding those belonging to the structure itself. The criteria adopted to identify and filter out the PSs associated with the stadium are detailed in the next section. This ensures that the inferred trend reflects only the large-scale ground motion and is not biased by local structural effects. Two alternative procedures, introduced in Chapter 3, are applied to these surrounding ground points to model the regional deformation.

Method 1 was applied to the ascending and descending datasets to derive a representative regional trend for the area surrounding the structure.
The comparison between regional and structural displacement time series shows only minor differences for both ascending and descending datasets (see Figure 4.10 and 4.11). This close agreement indicates that the structural measurements are still largely influenced by the regional deformation signal, which tends to mask the intrinsic structural behaviour.

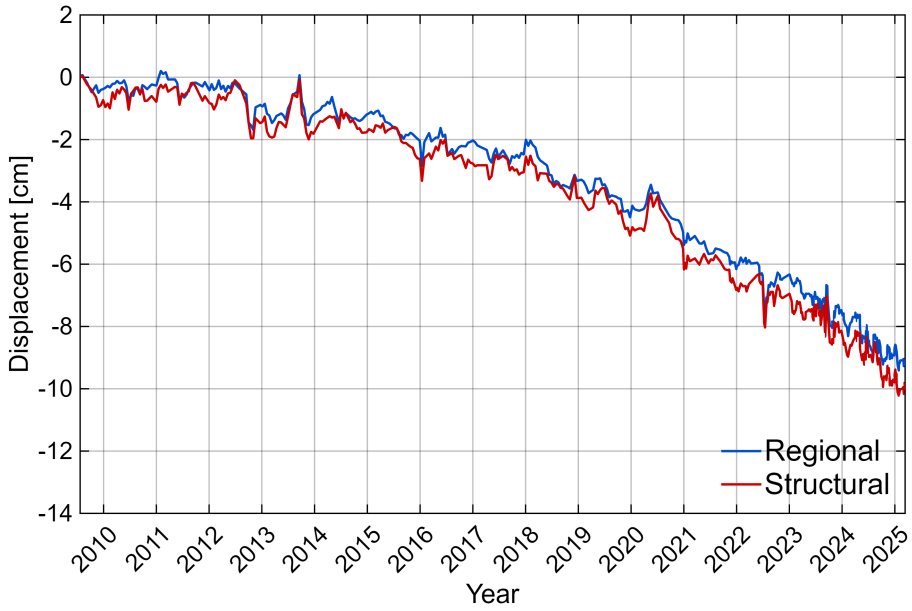

Figure 4.10: Method 1: Relative mean of regional points in blue and of structural points in red, ascending datasets.

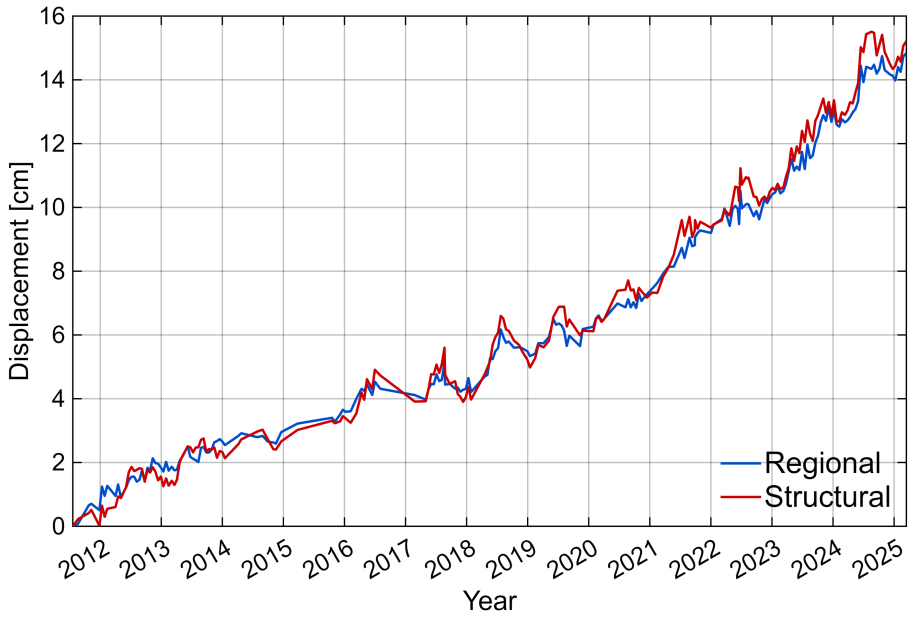

Figure 4.11: Method 1: Relative mean of regional points in blue and of structural points in red, descending datasets.

Method 2 was applied independently to the ascending and descending datasets to derive a parametric representation of the regional deformation affecting the area surrounding the structure. For each geometry, all displacement time series within the selected zone were pooled, and the constrained quadratic model was fitted to the aggregated data. The procedure was applied independently to ascending and descending acquisitions.

As shown in Figures 4.12 and 4.13, the computed values of the coefficient of determination R^2, are equal to 0.918 for the ascending dataset and 0.881 for the descending one.

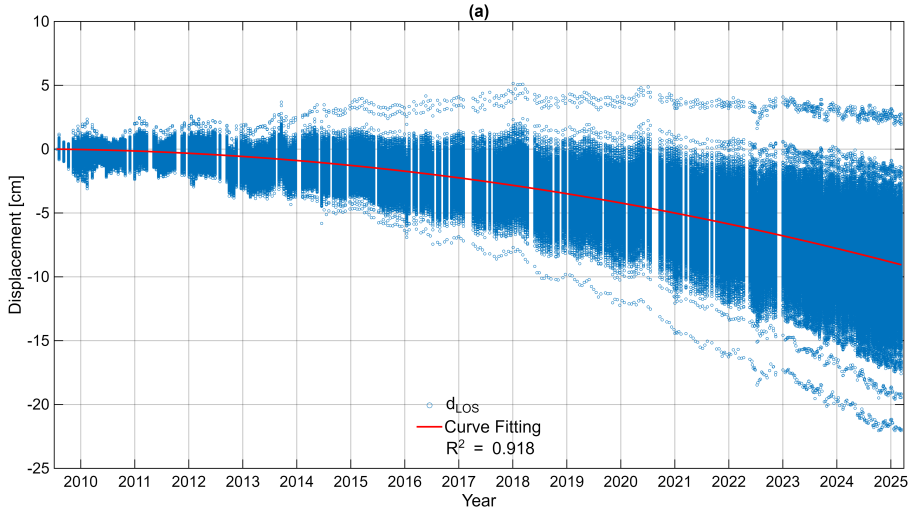

Figure 4.12: Constrained polynomial fit applied to the ascendent (a) and descendent (b) LOS displacement time series, showing the coefficient of determination R^2.

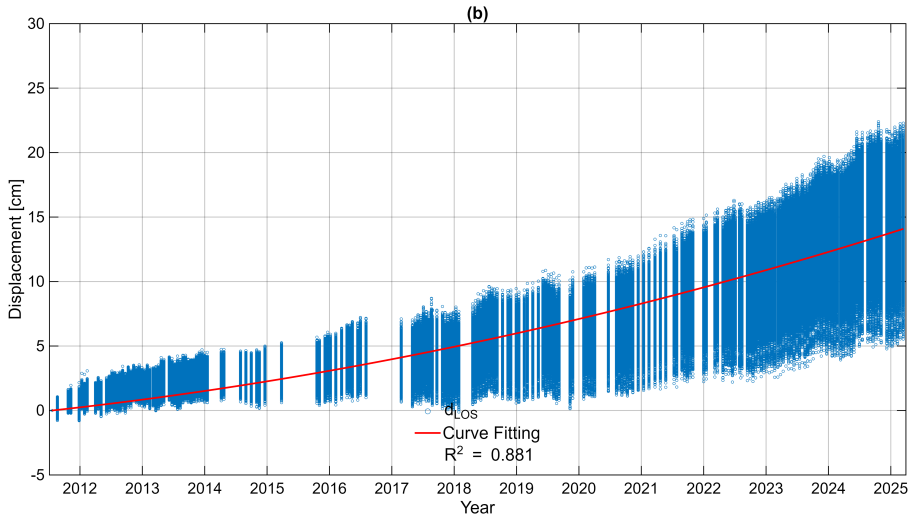

Figure 4.13: Constrained polynomial fit applied to the ascendent (a) and descendent (b) LOS displacement time series, showing the coefficient of determination R^2.

Figures 4.14 and 4.15 shows the comparison between the fitted regional curve and the mean displacement computed over the structure.

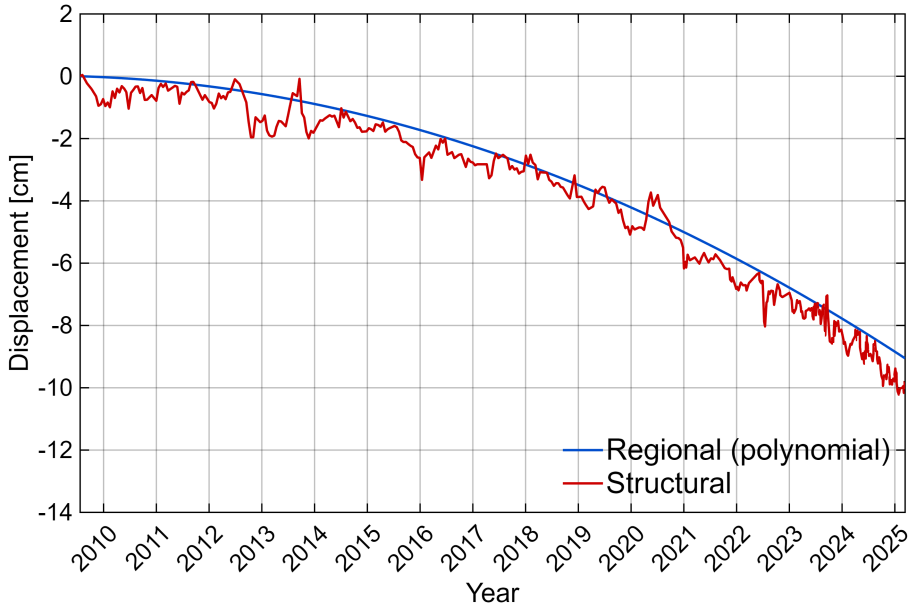

Figure 4.14: Polynomial curve of regional points in blue and Mean curve of structural points in red. Ascending datasets.

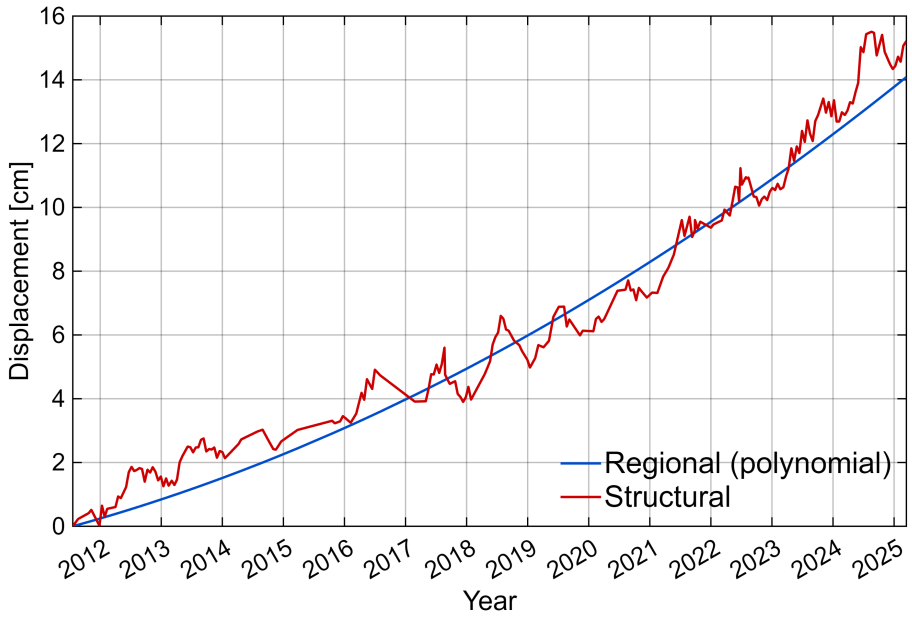

Figure 4.15: Polynomial curve of regional points in blue and Mean curve of structural points in red. Descending datasets.

4.4. Determination of structural displacements

This section describes the procedure adopted to derive structural displacements from the LOS time series of the PSs. First, PSs located in the vicinity of the stadium roof were first selected through a GIS-based workflow. A 10 m buffer was defined around the roof footprint, including both internal and immediately surrounding areas, excluding those that fall outside this footprints, in order to ensure adequate spatial coverage while maintaining relevance to the structural system.

An elevation filter was then applied to exclude ground-level points and retain only PSs associated with the roof. Since the available heights were expressed as ellipsoidal values (WGS84), they were converted to orthometric elevations using the local ellipsoid–geoid separation, which in the Naples area is approximately +50 m, with limited spatial variability. Only points located above 110 m were retained.

The filtered PSs were subsequently intersected with the predefined set of 28 structural clusters representing the roof elements. This step allowed each point to be assigned to a specific structural zone, for both ascending and descending geometries, ensuring a consistent spatial organisation of the dataset.

Finally, the regional subsidence component was removed from the LOS time series using the two approaches described in Chapter 3. Results are shown in Figure 4.16 and Figure 4.17.

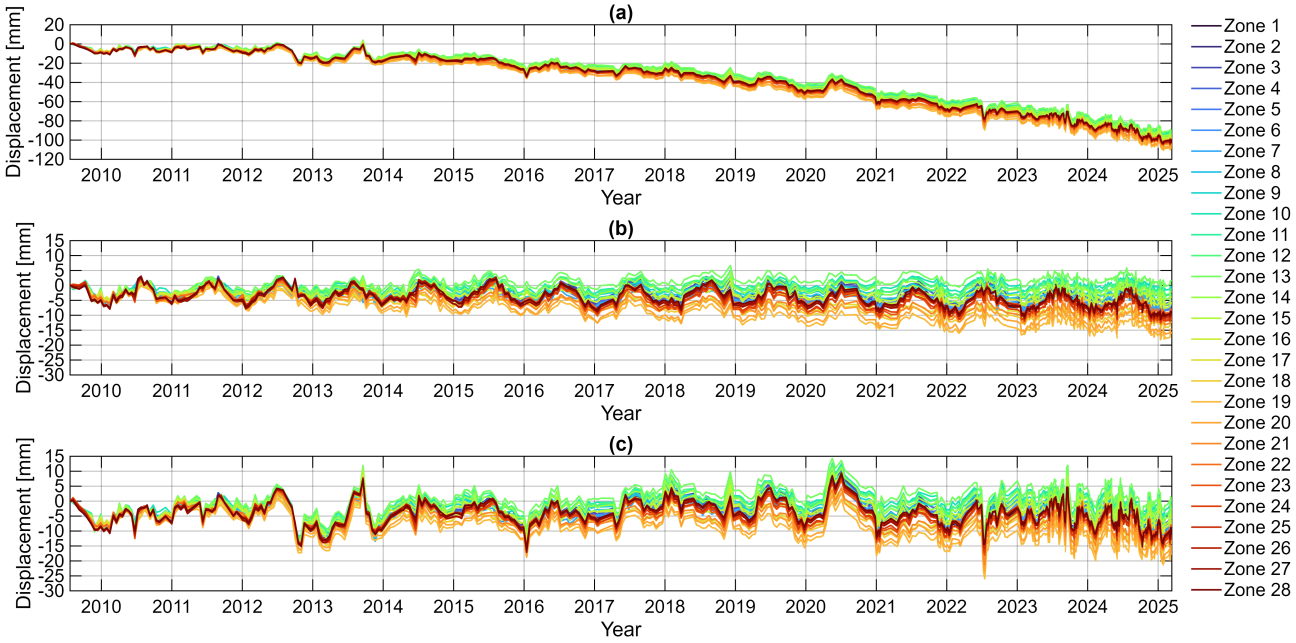

Figure 4.16: Displacement time series of the stadium roof elements for the ascending orbit not processed (a), processed using Method 1. (b), processed using Method 2 (c).

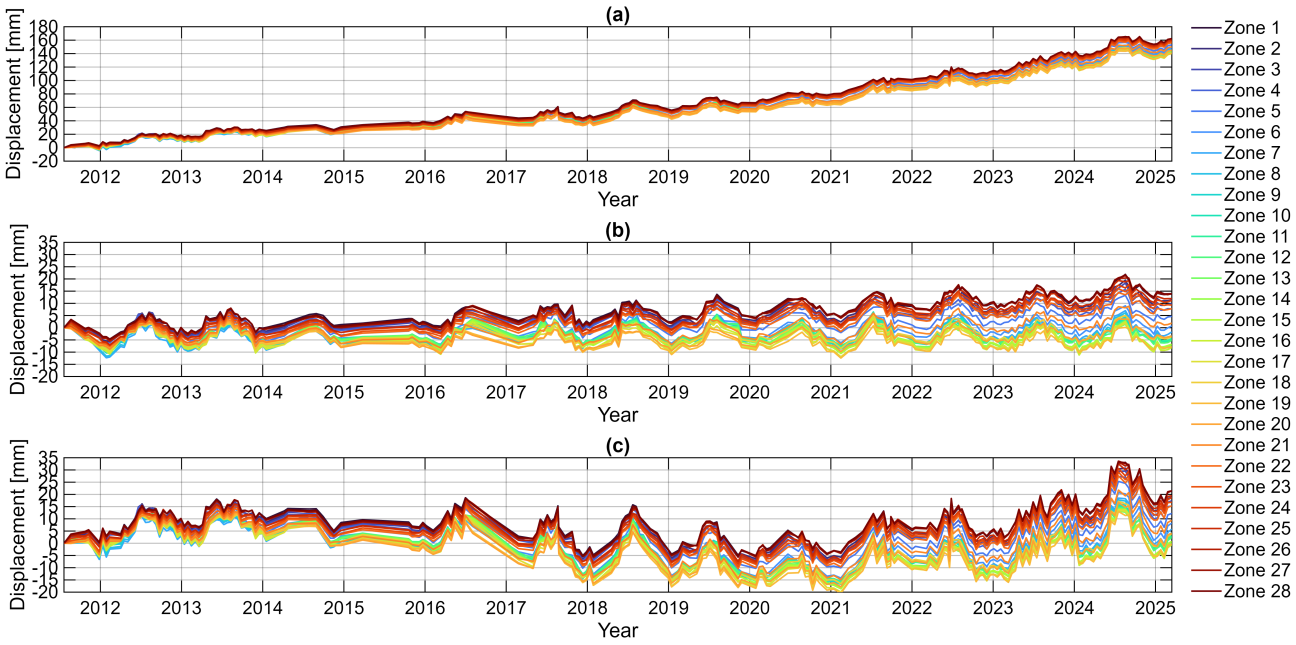

Figure 4.17: Displacement time series of the stadium roof elements for the descending orbit not processed (a), processed using Method 1. (b), processed using Method 2 (c).

The corrected displacement series were then compared with the original data for both acquisition geometries in order to evaluate the influence of the regional trend on the reconstructed structural behaviour. The comparison between the two corrected displacement series, one processed by subtracting the overall mean trend (Method 1), the other by removing a best fitting

curve (Method 2), reveals a persistent divergence in the resulting signals.
Since the roof trusses behave as longitudinal structural elements, it is convenient to transform these global components into a beam-aligned coordinate system. This is achieved by applying a rotation from the (E,N,U) frame to a local (L,T,U) system, where the L axis is oriented along the truss longitudinal direction, the T axis lies in the horizontal plane and is orthogonal to L, and the U axis corresponds to the vertical direction.
The orientation of each truss beam α_{Beam}, is obtained by tracing the beam axis on the planimetry and measuring, the clockwise angle between the East direction and the beam axis; a local reference frame is defined for each sector such that the longitudinal axis L is aligned with the beam and the transverse axis T is orthogonal to it.
The values of α_{Beam} computed for the 28 roof sectors are reported in the table below and showed in Figure 4.18. For clarity, the sectors are split into two adjacent columns: Zones 1–14 and Zones 15–28. This separation reflects the geometric behaviour of the truss system. In fact, starting from Zone 15, the beam orientation, measured clockwise from the East direction, returns to values close to zero degrees, meaning that these beams lie again just below the East axis.

Zone	α_{Beam} [°]	Zone	α_{Beam} [°]
1	183.3	**15**	4.2
2	196.4	**16**	17.4
3	210.0	**17**	31.0
4	226.0	**18**	46.7
5	245.3	**19**	64.8
6	266.3	**20**	86.7
7	286.6	**21**	106.6
8	306.3	**22**	124.9
9	322.8	**23**	142.1
10	338.3	**24**	156.6
11	345.0	**25**	165.2
12	349.3	**26**	168.2
13	353.1	**27**	172.0
14	357.5	**28**	176.2

Table 4.1: The truss orientation angle α_{Beam} values for the 28 roof zones.

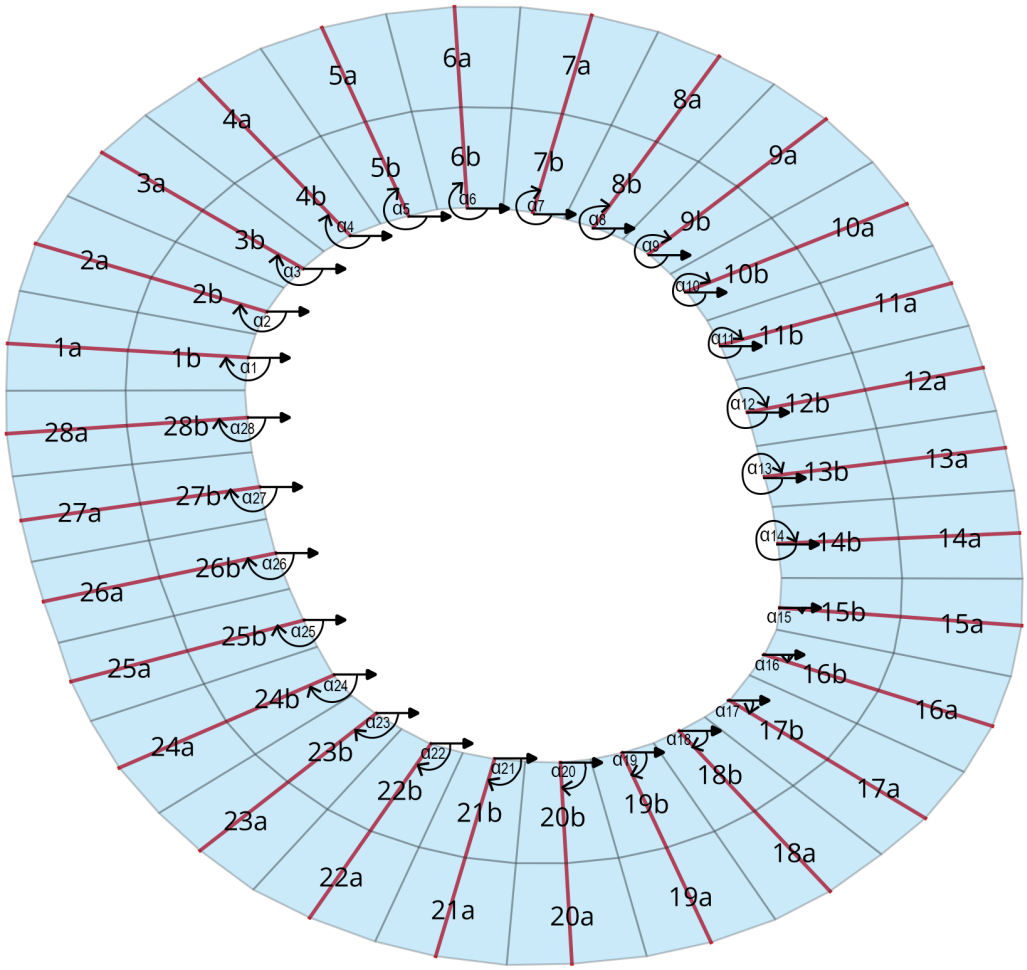

Figure 4.18: The truss orientation angle α_{Beam} for the 28 roof zones.

The azimuth of the Azimuth Looking Direction α_{ALD} can be derived for each orbit (ascending and descending). For the ascending dataset, the resulting azimuth is equal to 171.6°, whereas for the descending dataset the computed value is 11.0°.

Given the angles α_{Beam} and α_{ALD}, the rotation into the local (L,T,U) reference frame leads directly to the system of equations (21), which links the ascending and descending LOS measurements to the unknown longitudinal and vertical components of each structural sector. With these angles defined and the LOS displacements from both geometries available, the system can be solved to retrieve the longitudinal and vertical displacements for every zone.

The steps described above provide, for each roof sector, two independent estimates of the longitudinal and vertical structural displacements, obtained by applying the two subsidence filtering strategies. The resulting displacement components d_L are presented in Figure 4.19 and show that Method 2 exhibits greater short-term variability and more pronounced isolated peaks, whereas Method 1 produces smoother time histories with reduced high-frequency fluctuations. Because the sensitivity of the LOS geometry to longitudinal and vertical motion varies as a

function of α_{Beam}, the amplitude and shape of the reconstructed d_L and d_U time series differ across sectors.

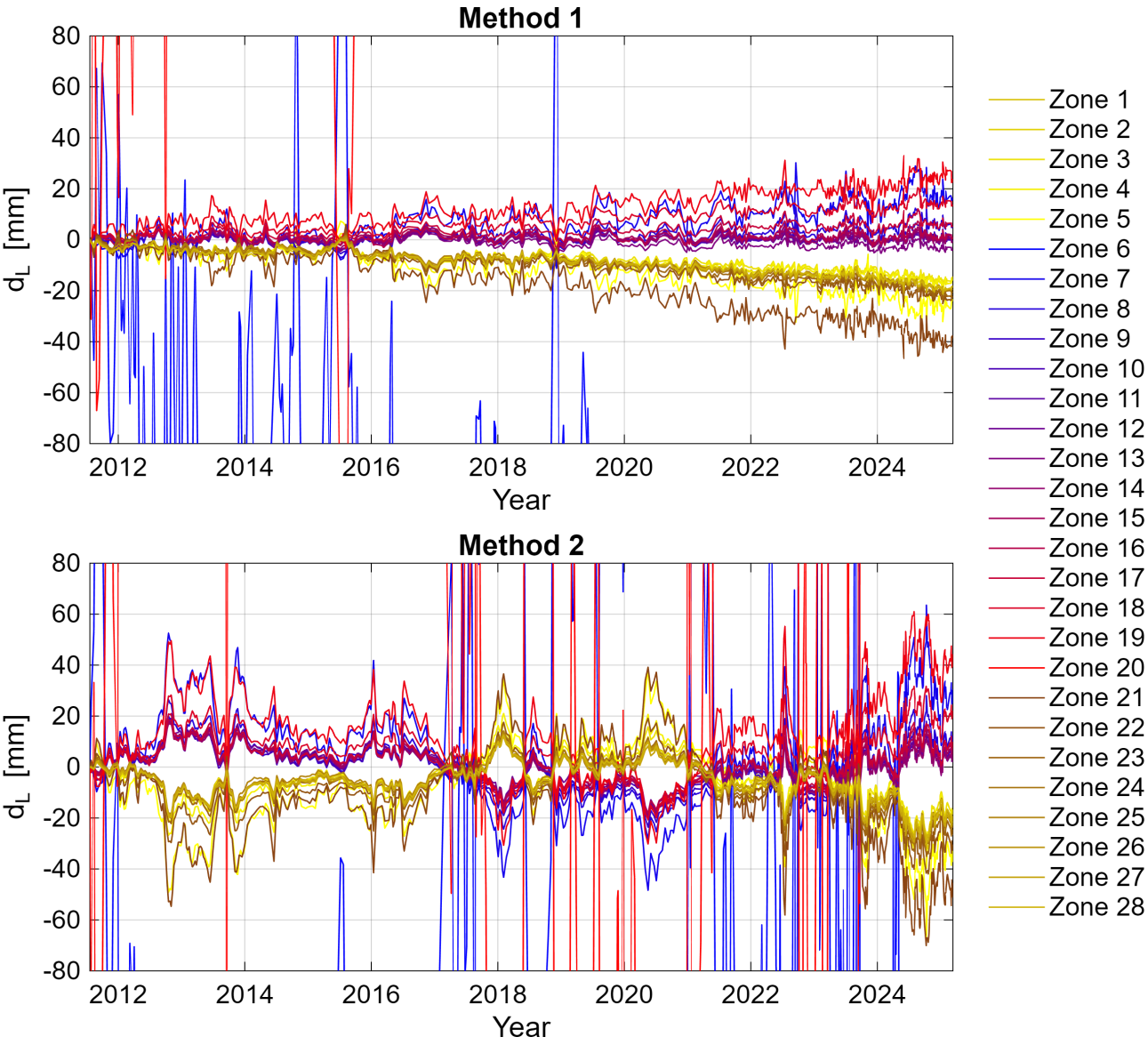

Figure 4.19: Longitudinal components d_L for all clusters (a), computed with Method 1 and Method 2.

A notable behaviour emerges in the northern and southern sectors (e.g., clusters 6 and 20, the red and blue series in Figure 4.19), where the reconstructed displacements exhibit unusually large amplitudes. This effect is not linked to the filtering method itself but to the geometric configuration: in these zones, the difference between the Azimuth Looking Direction angle and the beam orientation angle α_{Beam} becomes extremely small, causing the LOS projection to amplify the longitudinal component. This geometric sensitivity explains the sharp peaks observed in these specific sectors and highlights the importance of viewing geometry when interpreting the combined ascending–descending solutions. Removing the two series that present unreliable

displacements (clusters 6 and 20), the two methods can be compared more easily, and a clear sign change in d_L, caused by the reversal of the beam axis orientation relative to the satellite look direction, becomes evident across the remaining sectors.

Figure 4.20, which compares zones 7–19 for the two methods (a) and (b), and zones 21–5 for the two methods (c) and (d), a pattern emerges that mirrors the behaviour previously discussed. Since the goal is to extract the structural, low-frequency deformation signal while minimising geometry induced artefacts, method 1, yielding smoother and more coherent series across adjacent zones, is preferable. The figure also highlights the mathematical and geometric contrast between panels (a) and (c), and between (b) and (d): the time series of zones 7–19 and those of zones 21–5 do not share a uniform sign; rather, they display opposite trends, reflecting the opposite sign of the reconstructed longitudinal component. This inversion arises from the change in beam orientation and the corresponding variation in the α_{Beam} angle, which flips the direction of the projected longitudinal displacement.

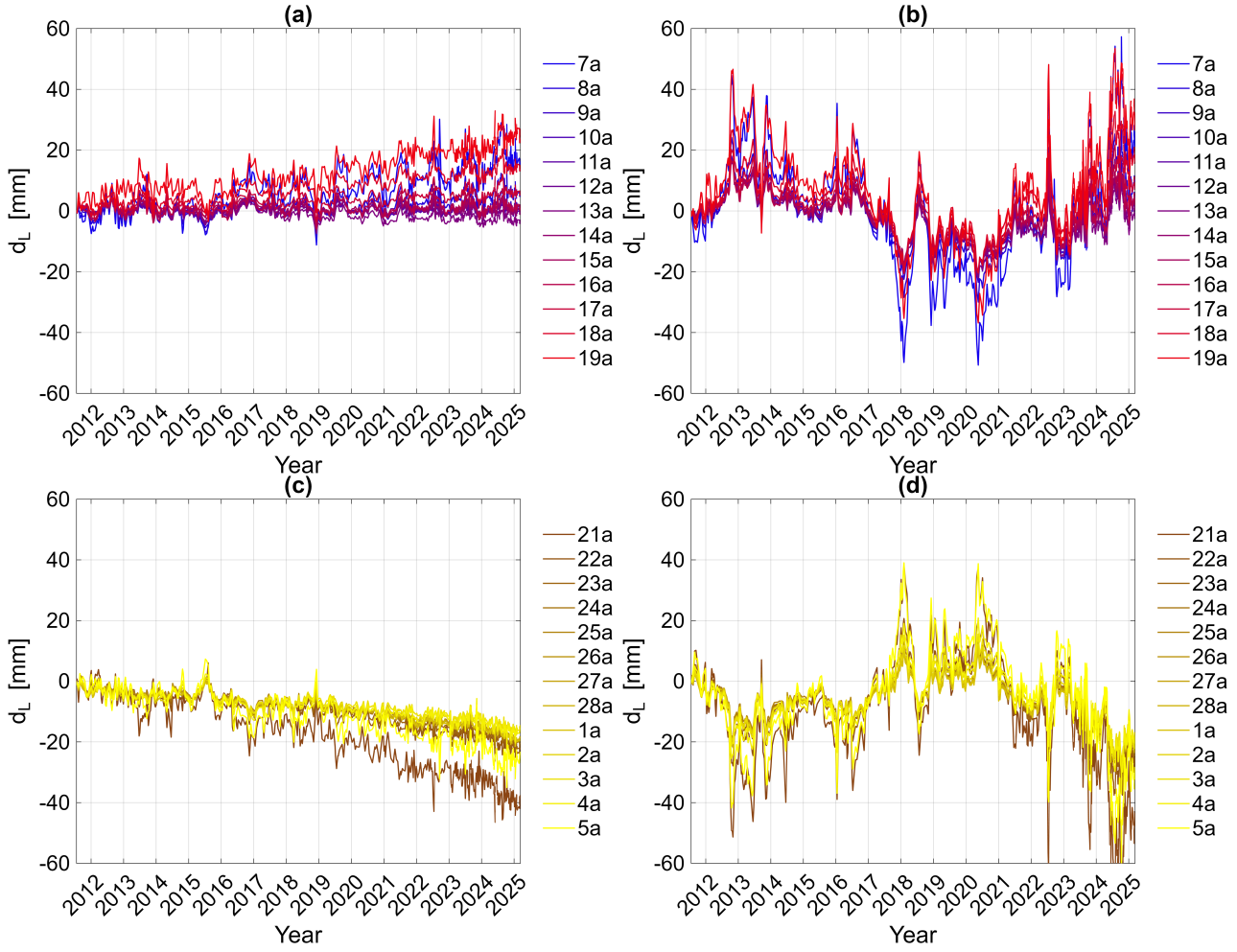

Figure 4.20: Longitudinal displacements d_L for zones 7–19 obtained with method 1 (a) and method 2 (b); d_L for zones 21–5 obtained with method 1 (c) and method 2 (d).

The vertical displacements d_U (see Figure 4.21) derived from both methods clearly show a pronounced seasonal cycle between winter and summer, consistent with thermic deformations of the structure: uplift and subsidence correlate with colder and warmer periods respectively. Although the two methods reproduce the same seasonal pattern, method 2 exhibits higher short term variability and therefore can be more sensitive to transient events; method 1 produces smoother, more coherent d_U series that better isolate the low-frequency structural signal and suppress geometry-induced noise.

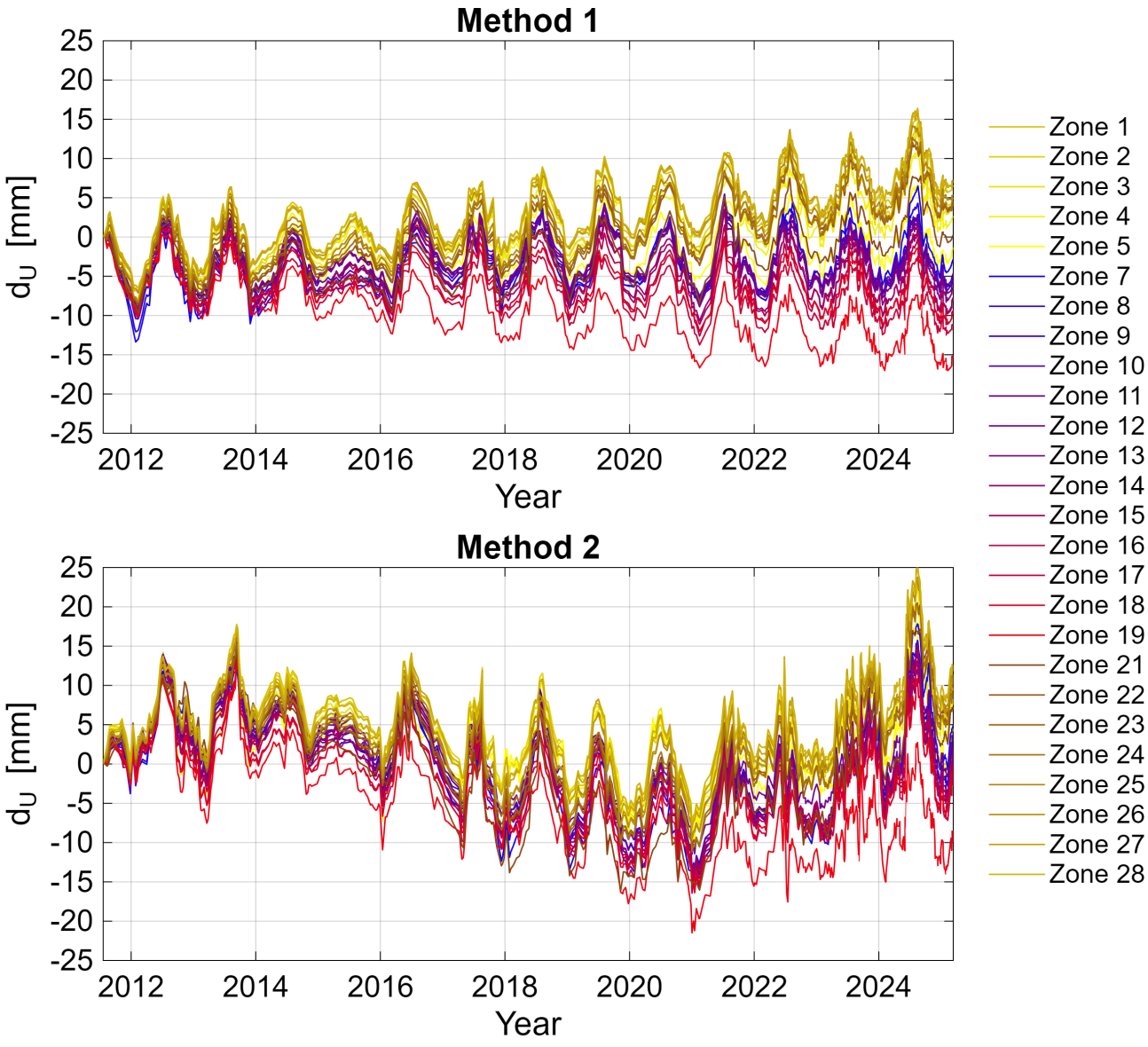

Figure 4.21: Vertical components d_U for all clusters (a) except zone 6 and 20, computed with Method 1 and Method 2.

Beyond the thermal cycle, the north western zones (26 to 5) show a progressive upward movement, whereas the south eastern zones (15 to 19) display the opposite behaviour, with a gradual

downward trend. The intermediate zones exhibit a more regular and less pronounced pattern. This asymmetry does not reflect an actual structural response but is attributable to an incomplete separation between the ground deformation component and the structural signal.
One possible reason for this incomplete separation lies in the choice of the area used to estimate the soil contribution, a 1 km^2 square surrounding the stadium. Such a broad selection may produce averaged values that do not accurately represent the local behaviour of the soil immediately adjacent to the structure. To address this issue, as illustrated in Figures 4.23 and 4.24, two soil portions adjacent to the stadium are analysed by selecting two clusters located near zones 1–5 and 15–19.

Figure 4.22: Clusters with soil points located near zones 1–5 and 15–19.

Selecting the soil PSs intersecting these clusters, the mean trend and the polynomial curve are computed. Following the same procedure adopted in the previous analysis, and combining the two orbital datasets, the d_U series for zones 1–5 and 15–19 obtained from the original 1 km^2 area are then compared with those derived from the new stadium-adjacent selection. This comparison is showed in Figures 4.23 and 4.24.

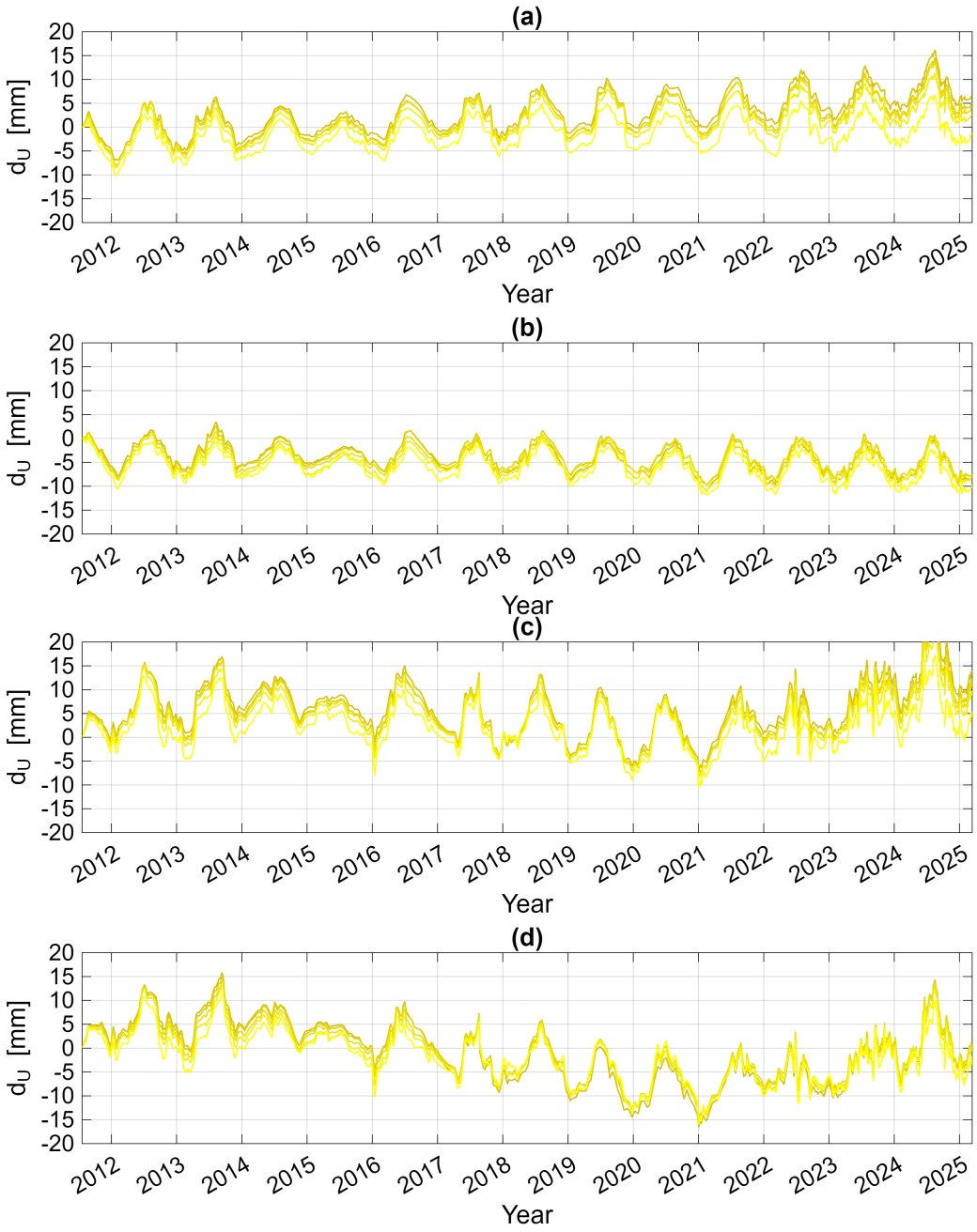

Figure 4.23: Vertical component d_U showed for zones 1 to 5. Processed with method 1 ((a) for 1 km^2 and (b) for adjacent soil points) and method 2 ((c) for 1 km^2 and (d) for soil points adjacent to the stadium).

By comparing panels (a) and (b) of Method 1, a clear improvement emerges when using adjacent soil points: the series in (b) appear more regular, compact, and stable. In particular, they no longer exhibit the upward drift previously observed in zones 1–5 or the downward trend of zones 15–19. This behavior highlights the influence of point selection on the resulting time series and shows that the use of adjacent points reduces local variability for this case study.

The comparison between panels (c) and (d) for Method 2 reveals only a modest improvement.

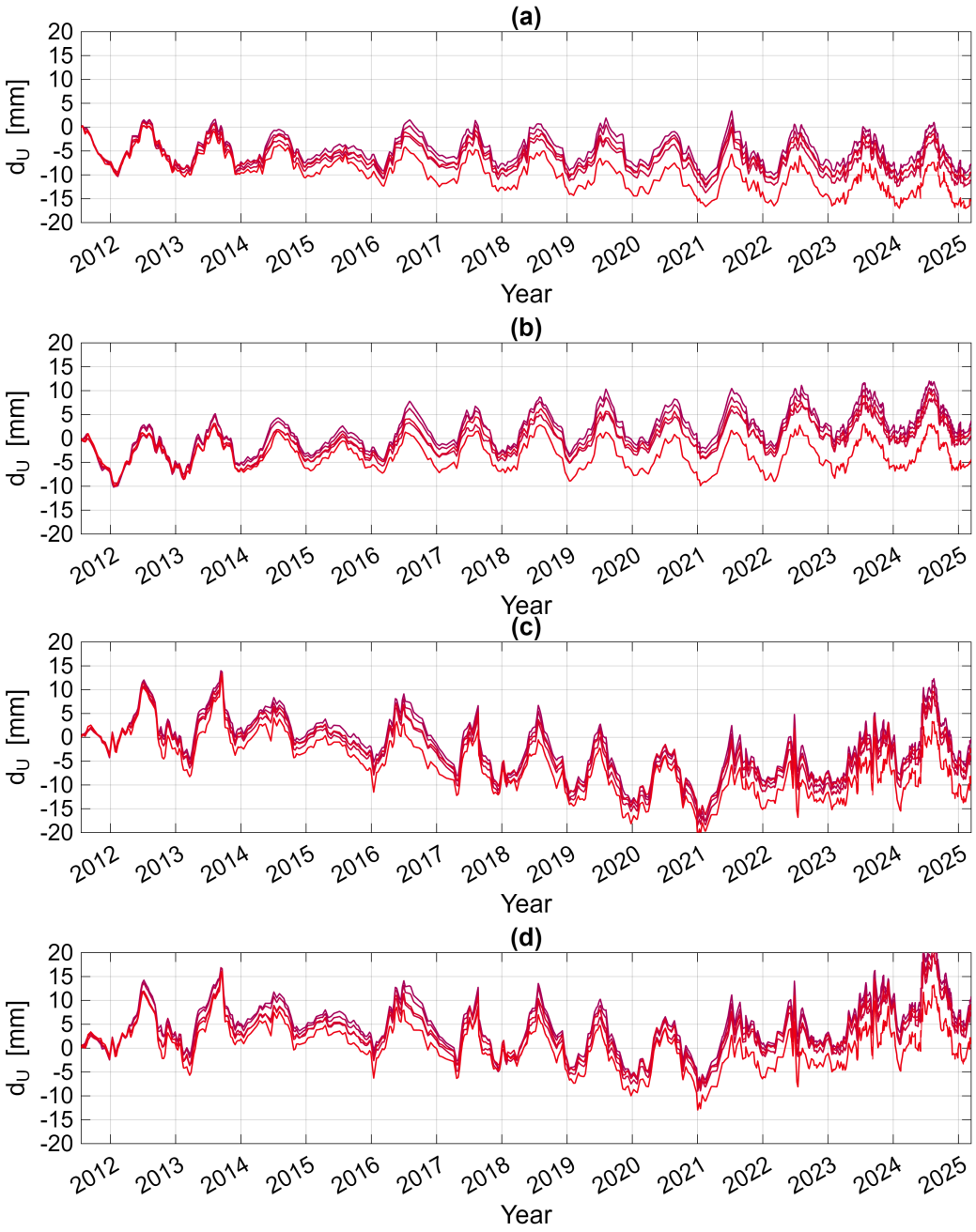

Figure 4.24: Vertical component d_U showed for zones 15 to 19. Processed with method 1 ((a) for 1 km^2 and (b) for adjacent soil points) and method 2 ((c) for 1 km^2 and (d) for soil points adjacent to the stadium).

The curves obtained from adjacent soil points are smoother and the enhancement is far less pronounced than in Method 1.

To further evaluate which method better captures the structural behaviour expected from thermal deformation, an additional comparison is introduced. Since no in-situ monitoring data are available and therefore no true benchmark exists, an hypotetical sinusoidal curve representing the thermal response of the structure is constructed. This curve is computed using

a set of estimated parameters representative of the environment and structural conditions, to determine the expected thermal elongation of a beam:

$$\Delta L = \alpha \, L \, \Delta T = 15 \, mm \tag{25}$$

where L = 41.65 m, is the length of a structural beam, $\alpha = 12 \times 10^{-6} \, \mathrm{C}^{\circ -1}$ is the thermal expansion coefficient of steel, $\Delta T = 30 \, \mathrm{C}^{\circ}$ corresponds to the estimated annual thermal excursion for the Naples area. From equation (25), the amplitude A of the sinusoidal displacement:

$$A = \frac{\Delta L \cdot 1000}{2} = 7.5 \, mm \tag{26}$$

and the final expression:

$$d_U(t) = A \, \sin(2\pi(X - x_0) + \phi) \tag{27}$$

This last equation describes the vertical displacement induced by the annual thermal cycle, with X denoting the time axis of the dataset, x_0 the reference year used for alignment, and ϕ the phase shift accounting for the seasonal delay between maximum and minimum temperatures, assumed in August and January. Figure 4.25 shows, as an example, the curve with vertical components d_U calculated using soil points in the 1 km^2 area. Having established this hypothetic benchmark, it becomes possible to perform a direct statistical comparison between the two processing methods, evaluating how their results differ when applied to the different soil dataset used in the analysis. The root mean square error (RMSE) between the hypothetical sinusoidal curve and the time series of each zone is then computed to quantify the deviation of the observed displacements from the reconstructed thermal behaviour, as reported in the next table for zones 1 to 5 and 15 to 19.

Zone	M1(a)	M1(b)	M2(a)	M2(b)
1a	5.94	3.71	9.43	5.85
2a	4.99	4.38	8.45	5.64
3a	4.66	4.43	8.07	5.40
4a	4.02	5.08	7.17	5.20
5a	3.43	6.74	5.10	5.16
15a	5.72	3.57	5.58	6.64
16a	6.76	3.25	6.05	5.99
17a	8.15	3.44	6.92	5.46
18a	7.08	3.34	6.01	6.16
19a	11.23	4.35	8.89	4.61

Table 4.2: RMSE values for Method 1 and Method 2 computed (a) over the 1 km^2 area and (b) over the soil points adjacent to the stadium, for zones 1 to 5 and 15 to 19.

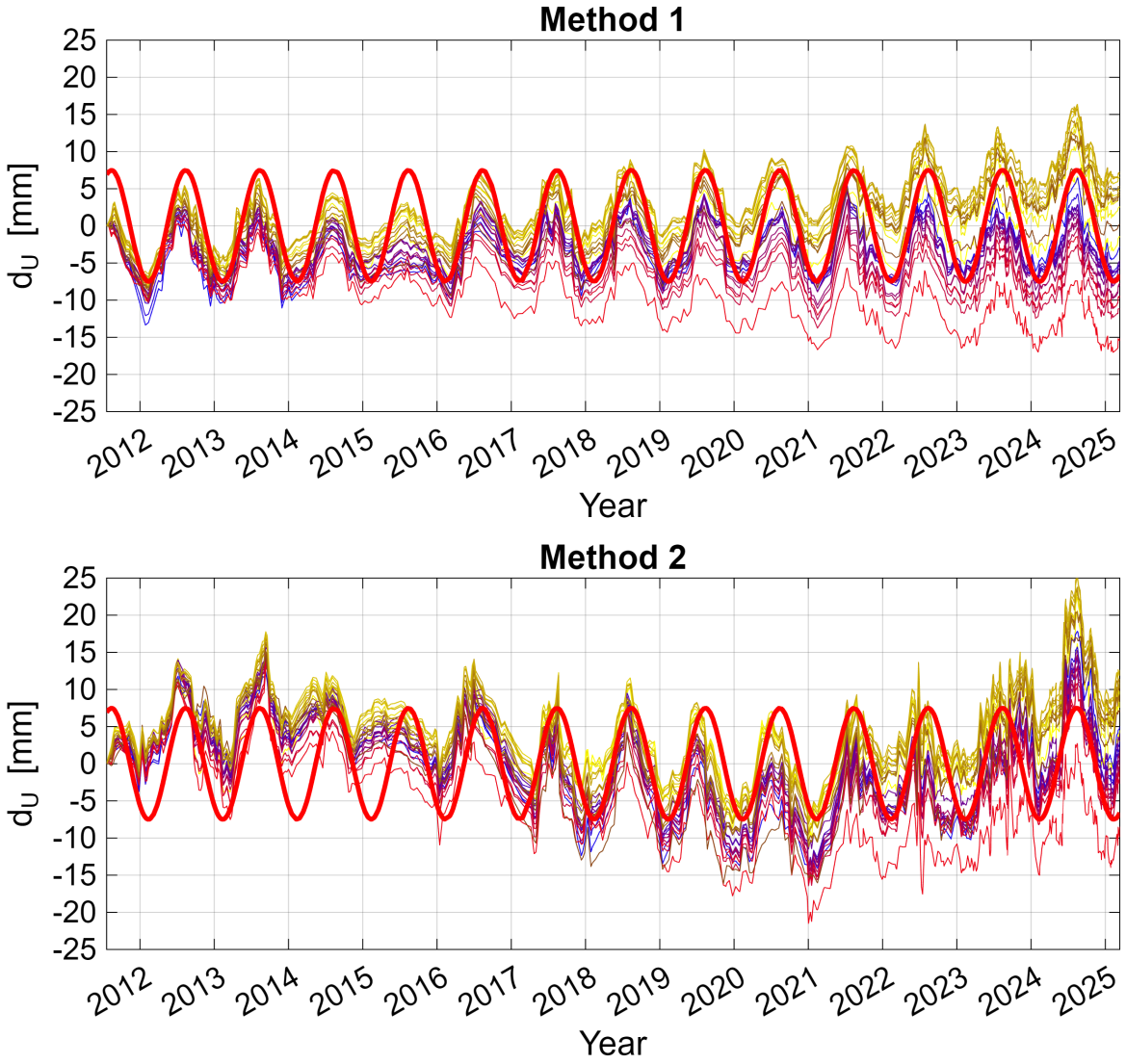

Figure 4.25: The hypotetical sinusoidal curve and vertical components d_U for all clusters (a) except zone 6 and 20, computed with Method 1 and Method 2, using soil points in the 1 km^2 area.

This metric provides an objective measure of how closely each method reproduces the expected structural response. The comparison of RMSE values confirms that Method 1 yields smaller deviations from the hypotetical thermal curve, indicating that it better captures the structural behaviour and represents the most reliable approach for isolating the low-frequency signal. The use of soil data from points adjacent to the structure further improves the accuracy of both methods, as reflected by the lower RMSE values.

In conclusion, the most robust configuration is obtained by applying Method 1 together with the adjacent-area soil PSs, as this pairing achieves the lowest RMSE values and therefore the most faithful reconstruction of the underlying structural response.

5 | Conclusions and future developments

Monitoring the integrity of large-span roofs is an increasingly complex challenge, exacerbated by material ageing, rising service loads and the growing influence of environmental and geological factors. In the case of the Diego Armando Maradona Stadium, located within the dynamic setting of the Campi Flegrei caldera, these difficulties are further amplified by the presence of regional ground deformation that can overlap with the structure's own movements. Within this context, the present work assessed the effectiveness of InSAR techniques for observing the behaviour of the stadium roof, analysing high-resolution COSMO SkyMed data and developing a dedicated methodology to separate geological effects from structural responses.

The preliminary analysis revealed that the raw interferometric signal is dominated by a strong regional component, coherent across the surrounding area, confirming the need for accurate subsidence removal before interpreting roof deformations. To this end, two approaches were implemented: one based on subtracting the relative mean of regional points, and another relying on a constrained polynomial model. Both successfully isolated the structural behaviour, although the former proved more stable and better suited for engineering interpretation.

Once the geological contribution was removed, the reconstruction of displacement components showed that the roof's response is strongly influenced by its elliptical geometry and by the varying orientation of its radial beams, confirming that satellite sensitivity changes significantly along the perimeter of the structure. The integration of ascending and descending orbits enabled the reconstruction of coherent longitudinal and vertical components, revealing a clear seasonal pattern attributable to thermal expansion of the steel elements.

It is worth noting that the adopted method, mostly applied to bridges, viaducts and infrastructures that develop primarily along a single longitudinal axis, was here adapted to a fundamentally different structural typology: an elliptical roof composed of radially oriented beams. The analysis of beam axes and the definition of a local reference system for each sector allowed a methodology typically used for linear structures to be extended to a far more articulated geometry, showing that, with appropriate geometric transformations, InSAR can also be employed for monitoring stadium roofs.

Nevertheless, to further validate the method and strengthen the interpretation of the results, it would be necessary to complement satellite analyses with structural models capable of simulating the thermal deformations of the roof, as well as with in-situ measurements enabling direct

and continuous comparison with InSAR-derived time series. The absence of such data currently limits the ability to distinguish expected thermal effects from potential local anomalies with absolute certainty. Despite this, the density of PSs, the internal consistency of the results and the repeatability of the observed trends confirm the robustness of the adopted approach. This work therefore highlights the potential of interferometric techniques as a complementary tool for monitoring large-span roofs in geologically active areas, while also emphasising the need for integration with physical models and local sensors to obtain a complete and reliable picture.
Future developments might involve expanding the methodology toward more comprehensive three-dimensional reconstructions, integrating thermo-structural modelling, and implementing semi-automatic pipelines capable of updating the analyses as new satellite acquisitions become available.
The results demonstrate that InSAR represents a reliable and non-invasive tool for the continuous surveillance of complex infrastructures, contributing to informed management and enhanced safety of major structures in dynamic environments such as the Campi Flegrei region.

Bibliography

[1] V.Macchiarulo, P.Milillo, C.Blenkinsopp, C.Reale, and G.Giardina. Multi-temporal insar for transport infrastructure monitoring: Recent trends and challenges. *Proceedings of the Institution of Civil Engineers - Bridge Engineering*, 176:92–117, 2023.

[2] V.Serlenga, M.Limongelli, A.Giordano, G.Foti, A.Montanaro, A.Santarsiero, and M.Santarsiero. An integrated approach for structural behavior characterization of the Gravina Bridge (Matera, Southern Italy). *Structural Health Monitoring*, 20(6):3371–3391, Nov 2021. doi: 10.1177/1475921720987544.

[3] D.Tonelli, M.Bonano, A.Mele, M.Silla, P.Striano, R.Lanari, M.DiLudovico, and A.Prota. Interpretation of Bridge Health Monitoring Data from Satellite InSAR Technology. *Remote Sensing*, 15(21):5242, Nov 2023. doi: 10.3390/rs15215242.

[4] Z.Masoumi, Z.Mousavi, and Z.Hajeb. Long-term investigation of subsidence rate and its environmental effects using the InSAR technique and geospatial analyses. *Geocarto International*, 37(24):7161–7185, Dec 2022. doi: 10.1080/10106049.2021.1964616.

[5] ReLUIS. *Linee guida per l'utilizzo dei dati interferometrici satellitari ai fini dell'interpretazione del comportamento strutturale delle costruzioni*, 2023.

[6] NASA. What is remote sensing?, 2023. URL `https://www.earthdata.nasa.gov/learn/backgrounders/remote-sensing`.

[7] G.Balsamo, R.de Rosnay, S.Beljaars, A.Prigent, A.Bartholomew, M.Di Giuseppe, A.McNally, J.Munoz-Sabater, L.Isaksen, J.Petersen, M.Drabek, and M.McCallum. Satellite and In Situ Observations for Advancing Global Earth Surface Modelling: A Review. *Remote Sensing*, 10(12):2–45, Dec 2018. doi: 10.3390/rs10122038.

[8] NASA. Active sensors, 2023. URL `https://www.earthdata.nasa.gov/learn/backgrounders/active-sensors`.

[9] G.Franceschetti and R.Lanari. *Synthetic Aperture Radar Processing*. Taylor and Francis Group, 1999. pp..

[10] R.Bamler. Principles of Synthetic Aperture Radar. *Surveys in Geophysics*, 21(2/3):147–157, 2000. doi: 10.1023/A:1006790026612.

[11] TRE ALTAMIRA. Materiale informativo, 2023. URL https://site.tre-altamira.com/. Adapted.

[12] S.Yalvac. Validating insar-sbas results by means of different gnss analysis techniques in medium- and high-grade deformation areas, 2020. URL https://www.researchgate.net/figure/SAR-acquisition-geometry-Dawson-et-al-2008_fig2_338640909.

[13] ReLUIS. *Linee guida per l'utilizzo dei dati interferometrici satellitari ai fini dell'interpretazione del comportamento strutturale delle costruzioni*, 2023. pp.7, Adapted.

[14] M.Crosetto, O.Monserrat, M.Cuevas-Gonzalez, N.Devanthery, and B.Crippa. Persistent Scatterer Interferometry: A Review. *ISPRS Journal of Photogrammetry and Remote Sensing*, 115:78–89, May 2016. doi: 10.1016/j.isprsjprs.2015.10.011.

[15] ESA. Ers at a glance, 2023. URL https://www.esa.int/Applications/Observing_the_Earth/ERS_at_a_glance.

[16] ESA. Ers-1 (european remote-sensing satellite-1), 2023. URL https://www.eoportal.org/satellite-missions/ers-1.

[17] ESA. Envisat (environmental satellite), 2023. URL https://www.eoportal.org/satellite-missions/envisat.

[18] ESA. Earth online: Envisat mission overview, 2023. URL https://earth.esa.int/eogateway/missions/envisat#instruments-section.

[19] ESA. Cosmo-skymed, 2023. URL https://www.eoportal.org/satellite-missions/cosmo-skymed#eop-quick-facts-section.

[20] A.Hooper, P.Segall, and H.Zebker. Persistent Scatterer Interferometric Synthetic Aperture Radar for Crustal Deformation Analysis, with Application to Volcán Alcedo, Galápagos. *Journal of Geophysical Research: Solid Earth*, 112(B7), Jul 2007. doi: 10.1029/2006JB004763.

[21] ReLUIS. *Linee guida per l'utilizzo dei dati interferometrici satellitari ai fini dell'interpretazione del comportamento strutturale delle costruzioni*, 2023. pp.7.

[22] ESA. Snap software, 2023. URL https://earth.esa.int/eogateway/tools/snap.

[23] A.Pepe, Y.Yang, M.Manzo, and R.Lanari. Improved EMCF-SBAS Processing Chain Based on Advanced Techniques for the Noise-Filtering and Selection of Small Baseline Multi-Look DInSAR Interferograms. *IEEE Transactions on Geoscience and Remote Sensing*, 53(8): 4394–4417, Aug 2015. doi: 10.1109/TGRS.2015.2396875.

[24] A.M.Ruiz-Armenteros, J.Martinez-Espla, J.Diaz, M.A.Fernandez, and J.M.Lopez-Sanchez. Multi-Temporal InSAR Processing Comparison in Presence of High Topography. *Procedia Computer Science*, 100:1181–1190, 2016. doi: 10.1016/j.procs.2016.09.278.

[25] K.Farova, J.Jelenek, V.Kopackova-Strnadova, and P.Kycl. Comparing DInSAR and PSI Techniques Employed to Sentinel-1 Data to Monitor Highway Stability: A Case Study of a Massive Dobkovicky Landslide, Czech Republic. *Remote Sensing*, 11(22):2670, Nov 2019. doi: 10.3390/rs11222670.

[26] F.Orellana and J.M.Delgado Blasco and M.Foumelis and P.J.V.D'Aranno and M.A.Marsella and P.Di Mascio. Dinsar for road infrastructure monitoring: Case study highway network of rome metropolitan (italy). *Remote Sensing*, 12(22):3697, Nov 2020. doi: 10.3390/rs12223697.

[27] R.Liuzzo. Satellite InSAR-based Monitoring of Critical Infrastructures: Application to Real Case Studies, 2020. pp. 33-45.

[28] P.F.Giordano, M.Kwapisz, A.Miano, R.Liuzzo, A.Vorwagner, M.P.Limongelli, A.Prota, and M.Ralbovsky. Monitoring of a multi-span prestressed concrete bridge using satellite interferometric data and comparison with on-site sensor results. *fib*, pages 5–13, 2025.

[29] P.F.Giordano, M.Kwapisz, A.Miano, R.Liuzzo, A.Vorwagner, M.P.Limongelli, A.Prota, and M.Ralbovsky. Monitoring of a multi-span prestressed concrete bridge using satellite interferometric data and comparison with on-site sensor results. *fib*, page 8, 2025. Adapted.

[30] EventInTour. Stadio diego armando maradona, 2023. URL `https://eventintour.com/venue/stadio-diego-armando-maradona/`.

[31] Ministero della Cultura. Scheda opera n. 3606, 2023. URL `https://censimentoarchitetturecontemporanee.cultura.gov.it/scheda-opera?id=3606`.

[32] Comune di Napoli. Stadio San Paolo - Archivi di UrbaNa, 2023. URL `https://www.comune.napoli.it/articolo_tematico/urbana-urbanistica-napoli/archivi-di-urbana/miscellanea/stadio/`.

[33] Archistadia. Napoli, lo stadio e il tetto in ferro: storia e caratteristiche, 2023. URL `https://archistadia.it/napoli-stadio-tetto-ferro-storia/`.

[34] Caoduro. Stadio San Paolo, 2023. URL `https://caoduro.it/realizzazioni/stadio-san-paolo/`.

[35] A.Fuccelli. Pianificazione Operativa 4D del Cantiere dello Stadio San Paolo mediante Metodologia BIM, 2018. pp. 2-10.

[36] Comune di Napoli. Masterplan Stadio Diego Armando Maradona, 2023. URL https://www.comune.napoli.it/novita/approvati-gli-indirizzi-per-gli-interventi-di-ammodernamento-funzionale-ed-energetico-dello-stadio-diego-armando-maradona/attachment/masterplan-stadio-maradona/.

[37] A.Fuccelli. Pianificazione Operativa 4D del Cantiere dello Stadio San Paolo mediante Metodologia BIM, 2018. pp. 6, Adapted.

Acknowledgements

Vorrei ringraziare la prof. Maria Giuseppina Limongelli, il prof. Pier Francesco Giordano e il Dott. Riccardo Liuzzo per la loro guida, supervisione e continuo supporto durante la realizzazione di questa tesi.

Un grazie speciale va ai miei genitori e a mio fratello per non avermi mai fatto mancare nulla e avermi lasciato libero di percorrere la mia strada.

Un grazie a tutta la famiglia per l'appoggio costante in questi anni di studio.

Un ringraziamento particolare al gruppo storico uscitelle, agli amici conosciuti durante il percorso di studi e ai miei coinquilini, una seconda famiglia.

Grazie a tutte queste persone che hanno contribuito a farmi crescere come persona affiancandomi durante questo faticoso ma gratificante percorso.

Grazie.